Inorganic Chemistry

Article

pubs.acs.org/IC

Molecular and Electronic Structure of Cyclic Trinuclear Gold(I) Carbeniate Complexes: Insights for Structure/Luminescence/Conductivity Relationships

Roy N. McDougald, Jr.,[†] Bhaskar Chilukuri,[†] Huiping Jia,[‡] Michael R. Perez,[‡] Hassan Rabaâ,[§] Xiaoping Wang,[†,∥] Vladimir N. Nesterov,[†] Thomas R. Cundari,*[,†] Bruce E. Gnade,*[,‡] and Mohammad A. Omary*[,†]

[†]Department of Chemistry, Center for Advanced Research and Technology (CART) and Center for Advanced Scientific Computing and Modeling (CASCaM), University of North Texas, Denton, Texas 76203, United States

[‡]Department of Materials Science and Engineering and Erik Jonsson School of Engineering and Computer Science, University of Texas at Dallas, Richardson, Texas 75083, United States

[§]Department of Chemistry, ESCTM, Ibn Tofail University, P.O. Box 133, Kenitra, 14000, Morocco

[∥]Chemical and Engineering Materials Division, Oak Ridge National Laboratory, Oak Ridge, Tennessee 37831, United States

Supporting Information

ABSTRACT: An experimental and computational study of correlations between solid-state structure and optical/electronic properties of cyclotrimeric gold(I) carbeniates, $[Au_3(RN{=}COR')_3]$ (R, R′ = H, Me, ^{n}Bu, or ^{c}Pe), is reported. Synthesis and structural and photophysical characterization of novel complexes $[Au_3(MeN{=}CO^nBu)_3]$, $[Au_3(^nBuN{=}COMe)_3]$, $[Au_3(^nBuN{=}CO^nBu)_3]$, and $[Au_3(^cPeN{=}COMe)_3]$ are presented. Changes in R and R′ lead to distinctive variations in solid-state stacking, luminescence spectra, and conductive properties. Solid-state emission and excitation spectra for each complex display a remarkable dependence on the solid-state packing of the cyclotrimers. The electronic structure of $[Au_3(RN{=}COR')_3]$ was investigated via molecular and solid-state simulations. Calculations on $[Au_3(HN{=}COH)_3]$ models indicate that the infinitely extended chain of eclipsed structures with equidistant Au--Au intertrimer aurophilic bonding can have lower band gaps, smaller Stokes shifts, and reduced reorganization energies (λ). The action of one cyclotrimer as a molecular nanowire is demonstrated via fabrication of an organic field effect transistor and shown to produce a p-type field effect. Hole transport for the same cyclotrimer—doped within a poly(9-vinylcarbazole) host—produced a colossal increase in current density from ~1 to ~1000 mA/cm^2. Computations and experiments thus delineate the complex relationships between solid-state morphologies, electronic structures, and optoelectronic properties of gold(I) carbeniates.

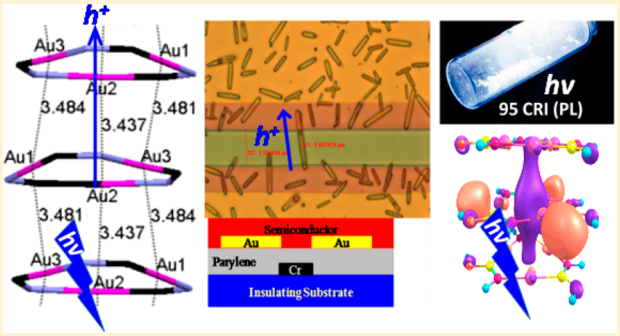

INTRODUCTION

Incorporation of a transition metal into organic materials can substantially impact their optical, electronic, and/or magnetic properties.[1] For example, cyclic trinuclear coinage metal complexes display a variety of photophysical properties including solvoluminescence, rigidochromism, and vapochromism.[2] The fundamental significance of cyclic trinuclear d^{10} complexes spans multiple areas of chemical bonding, such as metallophilic and excimeric bonding, π acid−base interactions, and metalloaromacity.[3] Mendizabal and co-workers have reported[3c−f] an interesting series of computational studies on weak interactions, including metallophilic bonding, involving gold and the other coinage metals. The focal points of this study are cyclic trinuclear gold carbeniate complexes, represented by $[Au_3(RN{=}COR')_3]$ (R and R′ are a selection of substituents) or Au_3Cb_3 (Au_3 and Cb_3 represent gold atoms and carbeniate ligands, respectively), which contain two-coordinate Au^I centers, connected by C═N bridging ligands, Chart 1.[4]

The photophysical and electronic properties of trinuclear Au^I complexes are impacted by solid-state intermolecular interactions that are mediated by aurophilic Au--Au interactions.[2,4,5] The extent of these intermolecular interactions are also modulated by the bulkiness of the ligand substituents (R, R′), which may retard or enhance intertrimer interactions, yielding structures of dimers of trimers, extended chains, *etc.*, in the solid state, as shown in Chart 2. Several examples of trimeric gold carbeniates have been reported.[1,6] Balch et al. elaborated on the $[Au_3(MeN{=}COMe')_3]$ series, for which steric bulk is

Received: April 8, 2014
Published: June 25, 2014

   dx.doi.org/10.1021/ic500808q | *Inorg. Chem.* 2014, 53, 7485−7499

Chart 1. Molecular Structure of the Trinuclear Gold(I) Carbeniate Complexes $[Au_3(RN{=}COR')_3]$[a]

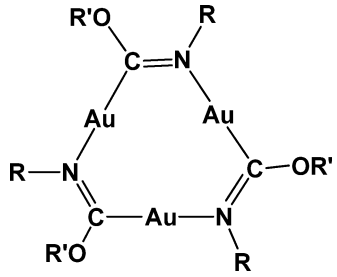

[a]R and R′ represent different substituents on the carbeniate ligands.

Chart 2. Stacking Arrangements Found in $[Au_3(RN{=}COR')_3]$ Complexes[a]

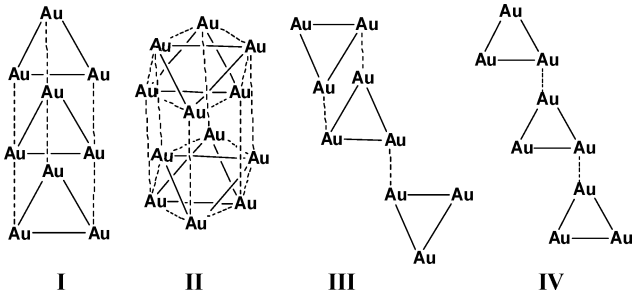

[a]Trinuclear complexes are represented by triangles, and intertrimer aurophilic interactions by dashed lines. Polymorphs are named as eclipsed (**I**), disordered staggered (**II**), chair conformation (**III**), and stair-step conformation (**IV**).

minimized by the use of methyl substituents.[4a,b] Aurophilic Au--Au interactions are hypothesized to lead to the formation of extended chains of trimers. Moreover, this pioneering research[4–6] demonstrated that the colorless solid of the hexagonal polymorph of $[Au_3(MeN{=}COMe)_3]$ displays an interesting solvoluminescence phenomenon:[4] upon prior irradiation of a crystalline sample with near-UV light, a bright burst of yellow light is observed spontaneously (remaining after irradiation stops) when solvent is introduced. The intensity of the luminescence is greatest for the best solvents for $[Au_3(MeN{=}COMe)_3]$, e.g., chloroform and methylene chloride.[4a] In the solid state, $[Au_3(MeN{=}COMe)_3]$ displays multiple crystalline polymorphs: hexagonal (*P6/m*) (which has eclipsed (**I**) and staggered (**II**) stacks), triclinic ($P\bar{1}$) (**III**), and monoclinic (*C2/c*) (Chart 2).[4b] Other polymorphic forms of gold carbeniate complexes, $[Au_3(^nPeN{=}COMe)_3]$ (**IV**) and $[Au_3(^iPrN{=}COMe)_3]$, with *n*-pentyl (^{n}Pe) and isopropyl (^{i}Pr) substituents were reported. These polymorphs differ in the way in which the trimer moieties interact with one another (Chart 2).

In the hexagonal form of $[Au_3(MeN{=}COMe)_3]$, which has a broad emission with a long-wavelength excitation and is the only form to display solvoluminescence, the trimers form two stack types, **I** and **II**, Chart 2.[4a] The hexagonal polymorph **I** shows an eclipsed stacking pattern with close Au--Au interactions forming a columnar extended chain, d_{Au-Au} = 3.346 Å *(intermolecular)* between pairs of trimers, and d_{Au-Au} = 3.308 Å (*intramolecular*) within the trimer. Polymorph **II** displays a staggered stacking pattern, resulting in dimers of trimers, where molecules are disordered with two positions of the trimers offset by 60° with d_{Au-Au} = 3.384 Å *(intermolecular)* and d_{Au-Au} = 3.280 Å (*intramolecular*). The triclinic polymorph **III** involves formation of dimers of trimers in a "chair" conformation with d_{Au-Au} = 3.339 Å *(intramolecular)* and d_{Au-Au} = 3.528 Å (*intermolecular*).[6] The monoclinic polymorph (**IV**) contains short prismatic stacks that consist of three trimers with d_{Au-Au} = 3.323 Å (*intramolecular*) and a single aurophilic connection between stacks of trimers, d_{Au-Au} = 3.653 Å (*intermolecular*).[4b]

Herein, we report our findings on the structural, photophysical, and conductive properties of the following novel complexes: $[Au_3(MeN{=}CO^nBu)_3]$, $[Au_3(^nBuN{=}COMe)_3]$, $[Au_3(^nBuN{=}CO^nBu)_3]$, and $[Au_3(^cPeN{=}COMe)_3]$, plus further investigation of the $[Au_3(MeN{=}COMe)_3]$ hexagonal polymorph (where ^{n}Bu = normal butyl and ^{c}Pe = cyclopentyl). The ^{n}Bu and ^{c}Pe substituents were used to increase the solubility of the trinuclear gold(I) carbeniate complexes, which could expand their uses in electronic devices. Additionally, the luminescence properties for each the complexes vary due to the nature of the aurophilic intermolecular interactions of each compound, which are augmented by the substituents. Due to a variety of photophysical properties of $[Au_3(RN{=}COR')_3]$ complexes bearing numerous polymorphic structures (Chart 2), based upon present and earlier[4–6] experiments, we report also a comprehensive computational study of different structural forms of Au_3Cb_3 complexes under both molecular and periodic regimes. In this research, we analyze the relationships between solid-state and molecular electronic structures and optoelectronic properties of these materials utilizing different polymorphic forms (Chart 2) as guidance. Simulations of the ground (singlet) and lowest excited (triplet) states are analyzed for molecular models to augment the search for important structure (molecular or solid)−property (electronic or optical) relationships that may guide the rational synthesis of novel materials for molecular electronic devices with both desired intramolecular and intermolecular arrangements.

RESULTS AND DISCUSSION

1. X-ray Crystallography of Gold Carbeniate Complexes. *Crystallographic Characteristics of $[Au_3(MeN{=}CO^nBu)_3]$.* The $[Au_3(MeN{=}CO^nBu)_3]$ colorless complex was obtained from a reaction of methyl isocyanide and potassium hydroxide with $(THT)Au^ICl$ in *n*-butyl alcohol (THT = tetrahydrothiophene). Crystals were grown from the slow evaporation of a dichloromethane solution of the complex, forming long needles. The X-ray data for the $[Au_3(MeN{=}CO^nBu)_3]$ complex are summarized in Figure 1 and Table 1. This complex crystallizes in a $P2_1/c$ space group and exhibits a stacking pattern akin to Balch's hexagonal polymorph **I** (Chart 2);[4a] that is, the individual planar molecules aggregate along the *c*-axis to form extended trigonal prismatic stacks. The Balch hexagonal polymorph stacks with the C atoms and N atoms of the ligand aligned throughout the prismatic stacks; for $[Au_3(MeN{=}CO^nBu)_3]$, the extended chain stacks contain alternating C and N atoms. The stacking motif between trimers shows Au--Au separations of ~3.43 Å.

All three of the *n*-butoxy groups lie almost parallel to the plane of the core nine-membered ring. The intramolecular Au−Au distances are 3.292(3), 3.297(3), and 3.280(3) Å. Other distances and angles are given in Table 2. As anticipated, the center geometry of the nine-membered $Au_3C_3N_3$ ring in this trinuclear complex is similar to that of the $[Au_3(MeN{=}COMe)_3]$ and the other novel complexes reported below.[4a]

dx.doi.org/10.1021/ic500808q | Inorg. Chem. 2014, 53, 7485−7499

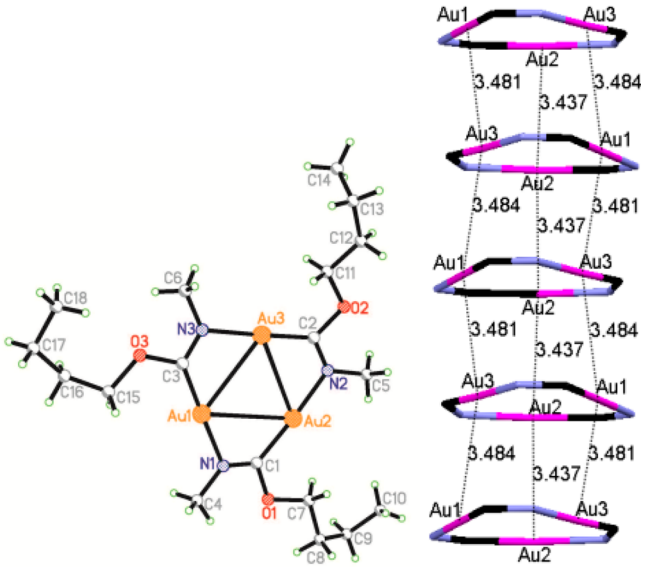

Figure 1. (Left) Crystal structure of $[Au_3(MeN{=}CO^nBu)_3]$. (Right) Molecule stacking orientation (pink = Au, blue = N, black = C).

Figure 1 shows the molecules interact to form an extended chain arrangement. Each of the molecules in the complex forms three Au--Au contacts with one molecule above and with one molecule below. This gives a total of six short Au--Au intermolecular interactions with distances ranging from 3.437 to 3.484 Å. The crystal was more stable at room temperature than at lower temperatures and the ^{n}Bu groups were disordered; see CIF file.

Crystallographic Characteristics of $[Au_3(^nBuN{=}COMe)_3]$. The colorless $[Au_3(^nBuN{=}COMe)_3]$ complex was obtained from a reaction of *n*-butyl isocyanide and potassium hydroxide with (THT)Au^{I}Cl in methanol. Crystals were grown from the slow evaporation of a dichloromethane solution of the complex, forming short needles. This complex crystallizes in a $P2_1/c$ space group, where a dimer-of-trimer unit exhibits a stair-step pattern (**IV**, Chart 2). The stacking motif between trimers shows alternating Au--Au distances of 3.517 and 3.675 Å, Figure 2.

The X-ray data for the $[Au_3(^nBuN{=}COMe)_3]$ complex are summarized in Figure 2 and Table 1. All three of the *n*-butyl groups lie parallel to the plane of the core nine-membered ring. The intramolecular Au−Au distances are 3.2656(4), 3.3218(5), and 3.3328(5) Å. Other distances and angles are given in Table 2. Figure 2 shows that each molecule interacts with one other molecule, forming a dimer of trimers, each of which has one Au--Au contact with a distance of 3.517 Å and a long Au--Au distance of 3.675 Å. The alternating Au--Au distances allow a loose chain interaction between the dimers of trimers, although the longer Au--Au distance is on the borderline of usual aurophilic interactions, typically found between 3.2 and 3.7 Å.[5]

Crystallographic Characteristics of $[Au_3(^nBuN{=}CO^nBu)_3]$. The colorless $[Au_3(^nBuN{=}CO^nBu)_3]$ complex was obtained from a reaction of *n*-butyl isocyanide and potassium hydroxide with (THT)Au^{I}Cl in *n*-butyl alcohol. Crystals were grown from the slow evaporation of a dichloromethane solution of the complex, forming long needles. This complex crystallizes in a $P\bar{1}$ space group, with two independent molecules in the unit cell.

Figure 3 shows the molecules interact to form an extended chain arrangement. Each of the molecules in the complex forms one Au--Au contact with one molecule above and one with the molecule below, yielding a total of two short Au--Au intermolecular interactions, with alternating Au--Au distances of 3.435 and 3.443 Å. The alternating short Au--Au distances allow an extended chain interaction between the molecules.

Crystallographic Characteristics of $[Au_3(^cPeN{=}COMe)_3]$. The $[Au_3(^cPeN{=}COMe)_3]$ colorless complex was synthesized and crystallized in a similar manner to the aforementioned complexes. This complex crystallizes in a $P\bar{1}$ space group, where dimers of trimers exhibit a chair-like pattern (**III**, Chart 2). The stacking motif between trimers shows two Au--Au distances of 3.446 Å.

Table 1. Crystallographic Data for Trinuclear Gold(I) Carbeniate Compounds

	V $[Au_3(MeN{=}CO^nBu)_3]$	**VI** $[Au_3(^nBuN{=}COMe)_3]$	**VII** $[Au_3(^nBuN{=}CO^nBu)_3]$	**VIII** $[Au_3(^cPeN{=}COMe)_3]$
cryst syst	monoclinic	monoclinic	triclinic	triclinic
color/habit	colorless needle	colorless needle	colorless needle	colorless needle
formula	$C_{18}H_{36}Au_3N_3O_3$	$C_{18}H_{36}Au_3N_3O_3$	$C_{27}H_{54}Au_3N_3O_3$	$C_{21}H_{36}Au_3N_3O_3$
fw	933.40	933.40	1059.63	969.43
space group	$P2_1/c$	$P2_1/c$	$P\bar{1}$	$P\bar{1}$
a (Å)	15.198(6)	22.7074(17)	10.611(5)	9.0763(11)
b (Å)	25.289(10)	9.0981(7)	14.342(6)	12.0289(15)
c (Å)	6.872(3)	23.2784(17)	21.393(9)	12.6926(16)
α (deg)	90	90	85.863(6)	62.098(2)
β (deg)	103.023(5)	104.347(1)	83.913(5)	85.009(2)
γ (deg)	90	90	87.780(5)	72.600(2)
V (Å^3)	2573.3(17)	4659.2(6)	3227(2)	1166.3(3)
Z	4	8	4	2
T (K)	296(2)	100(2)	100(2)	100(2)
λ (Å)	0.710 73	0.710 73	0.710 73	0.710 73
ρ_{calcd} (mg/m^3)	2.409	2.661	2.181	2.760
μ (cm^{-1})	17.081	18.868	13.634	18.849
R_1 [$I > 2\sigma(I)$]	0.0895	0.0272	0.0591	0.0383
wR_2 [$I > 2\sigma(I)$]	0.2353	0.0550	0.1162	0.0721
R_1 (all data)	0.1836	0.0424	0.1927	0.0804
wR_2 (all data)	0.3008	0.0605	0.1587	0.0857

dx.doi.org/10.1021/ic500808q | Inorg. Chem. 2014, 53, 7485−7499

Table 2. Selected Interatomic Distances (Å) and Angles (deg) for Trinuclear Gold(I) Complexes

	V $Au_3(MeN{=}CO^nBu)_3$	VI $Au_3(^nBuN{=}COMe)_3$	VII $Au_3(^nBuN{=}CO^nBu)_3$	VIII $Au_3(^cPeN{=}COMe)_3$
Au−C	1.94(4)	1.991(8)	1.929(9)	2.001(12)
	1.97(3)	1.984(8)	1.93(3)	1.987(12)
	1.88(4)	1.989(8)	1.95(2)	1.971(12)
Au−N	2.09(3)	2.053(6)	2.031(15)	2.069(9)
	2.02(4)	2.059(6)	2.009(17)	2.062(10)
	2.10(4)	2.029(6)	2.067(15)	2.046(9)
C=N	1.19(4)	1.312(10)	1.339(9)	1.280(14)
	1.30(4)	1.300(10)	1.335(10)	1.257(15)
	1.28(5)	1.291(10)	1.30(2)	1.289(15)
Au−Au(intra)	3.292(3)	3.2656(4)	3.2907(16)	3.2691(7)
	3.297(3)	3.3218(5)	3.3044(15)	3.3210(7)
	3.280(3)	3.3328(5)	3.2920(17)	3.2904(7)
C−Au−N	179(2)	178.5(3)	177.1(7)	177.0(4)
	176(2)	178.7(3)	178.4(8)	177.9(5)
	178(1)	177.6(3)	176.1(8)	175.4(4)

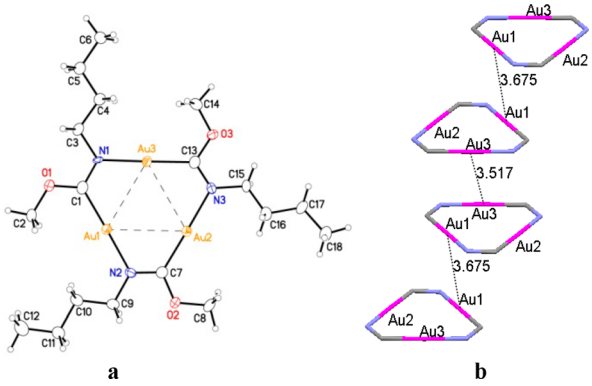

Figure 2. (a) Crystal structure of $[Au_3(^nBuN{=}COMe)_3]$. (b) Molecule stacking orientation (pink = Au, blue = N, gray = C).

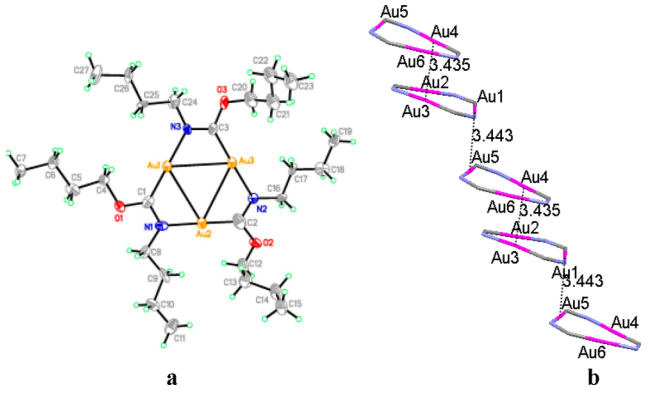

Figure 3. (a) Crystal structure of $[Au_3(^nBuN{=}CO^nBu)_3]$. (b) Molecule stacking orientation (pink = Au, blue = N, gray = C).

The solid-state structure of $[Au_3(^cPeN{=}COMe)_3]$ has one trinuclear complex in the asymmetric unit. The X-ray data for the $[Au_3(^cPeN{=}COMe)_3]$ complex are summarized in Figure 4 and Table 1. All three of the cyclopentyl groups are out of the plane of the core nine-membered $Au_3C_3N_3$ ring, with two angled up and one angled down. The intramolecular Au−Au distances are 3.2691(7), 3.3210(7), and 3.2904(7). Other distances and angles are given in Table 2.

Figure 4 shows that each molecule interacts with one other molecule, forming a dimer of trimers. Each dimer of trimers has two Au--Au contacts with a distance of 3.466 Å and has a long

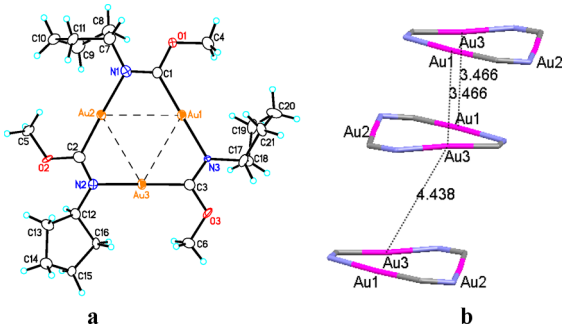

Figure 4. (a) Crystal structure of $[Au_3(^cPeN{=}COMe)_3]$. (b) Molecule stacking orientation (pink = Au, blue = N, gray = C).

Au--Au distance of 4.438 Å to neighboring molecules. The long Au--Au distance is considerably longer than typical aurophilic interactions of 3.2 to 3.7 Å.

An interesting solid-state structural difference between Balch's complex,[4a] polymorph **I** (Chart 2), and our (Figure 1) extended stacks arises from the asymmetric, μ-N,C nature of the carbeniate ligand. Even for identical substituents (i.e., R = R′), and in an eclipsed conformation, one may alternatively arrange the ligands head-to-head (H−H), i.e., with the ligating N atoms lined up along the columnar, trigonal prismatic stack, or head-to-tail (H−T), i.e., with ligating C and N atoms alternating along the columnar stacks (Chart 3).

We hypothesized that differences in electronegativity between carbon and nitrogen might yield an advantage to the H−T arrangement, i.e., enhanced electrostatic and/or dipole−dipole ($C^{\delta+}{=}N^{\delta-}/N^{\delta-}{=}C^{\delta+}$) attraction, to augment aurophilic Au--Au interactions. To assess this hypothesis in the solid state, the Cambridge Structural Database (CSD)[8] was searched for C=N···C=N close contacts of 3−4 Å (bond centroid to bond centroid distance). To avoid complications due to different sized metals and from ionic systems (e.g., differences in counterion properties), focus was given to neutral, organic molecules with C=N moieties in which C was three-coordinate and N two-coordinate. To focus attention on the most reliable crystal structures, the search was limited to *R* values of <5% and those without disorder or errors and excluded polymeric materials. For these two interacting bonds, the centroid-to-centroid separation was tabulated, as was the N=C···C=N dihedral (τ). For the latter metric, H−H is defined as $\tau \approx 0 \pm 10°$ and H−T as $\tau \approx 160$−$180°$. Two

dx.doi.org/10.1021/ic500808q | Inorg. Chem. 2014, 53, 7485−7499

Chart 3. (Left) Pictorial Description of the Head-to-Head (H−H), V, and (Right) Head-to-Tail (H−T), VI, Arrangement of Columnar Stacks

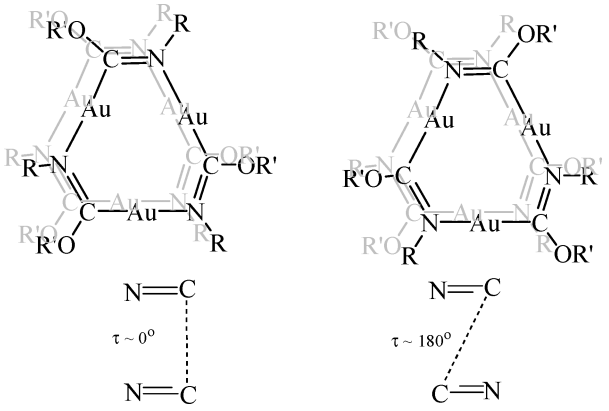

observations from this database analysis support the greater favorability of H−H versus H−T interactions among N═C functionalities. First, for the same 20° range of N═C···C═N dihedrals, *there are more than double the number of observations within the 3−4 Å range defined as a close contact for H−H versus H−T orientation*. Second, for these contacts the average (and median) distance is 3.8 Å for H−H (1662 observations) and 3.7 Å for H−T (3754 observations). The results of this solid-state structural analysis thus support the contention that electrostatic/dipole interactions in carbeniate and related asymmetric N,C-ligating ligands may provide an additional feature to be exploited to engineer crystal structures with these promising optoelectronic materials. We will return to this point below as the extent to which shorter trimer−trimer separations impact calculated HOMO−LUMO/VB−CB gaps (and thus electronic and optical properties) is investigated for Au_3Cb_3 materials (HOMO = highest occupied Kohn−Sham molecular orbital; LUMO = lowest unoccupied molecular orbital; VB = valence band; CB = conduction band).

2. Photoluminescence and Electrical Conductivity Properties of Gold Carbeniate Complexes. The complex $[Au(MeN{=}COMe)]_3$ (Chart 1, where R = R′ = Me), originally prepared by Balch and co-workers,[4a] shows a broad emission in the solid state across the visible spectrum in the range 400−700 nm and an excitation band that extends to 425 nm. The data collected in our laboratory and displayed in Figure 5a are consistent with those originally reported for the Balch complex[4a] with a slight variation in the relative intensity of the two emission bands. The broad dual emission causes the complex to render white light with an excellent color-rendering index (CRI) of 95, which is important for solid-state lighting applications of such materials because a single phosphor that exhibits white light will ameliorate differential aging and color binning problems in organic and inorganic light-emitting diodes (OLEDs and LEDs, respectively). The dual emission is composed of (i) a blue-turquoise component that is related to direct band gap emission where small contractions take place in intermolecular Au--Au distances upon excitation (*vide infra*), resulting in a relatively small (~3000 cm^{-1}) Stokes shift, and (ii) an orange-red component with a much larger (~8000 cm^{-1}) Stokes shift, attributed to self-trapped excitons that form within disordered stacks, giving rise to molecule-like emission. The molecule-like emission is likely due to the excitation of dimer-of-trimer subunits, akin to Yersin's model for a Pt(II)

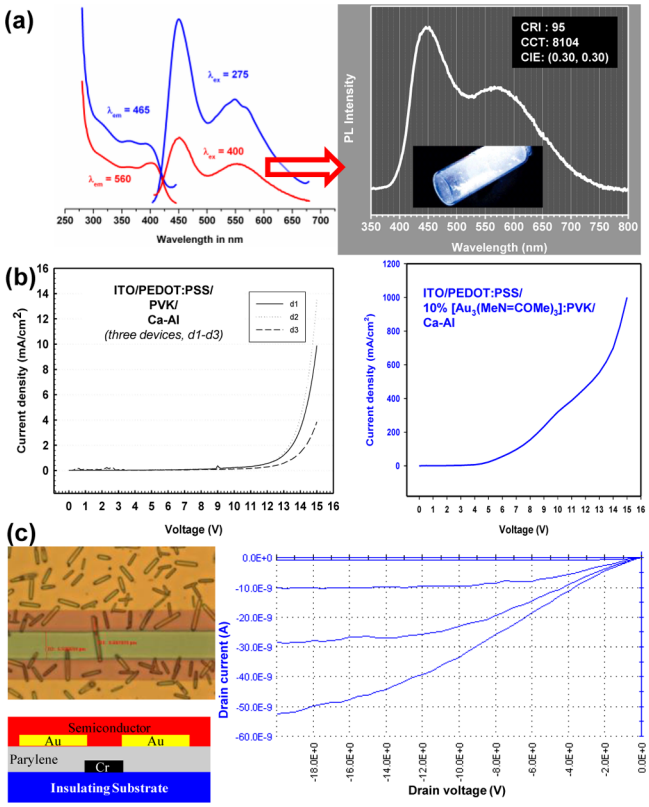

Figure 5. (a, top panels) Solid-state photoluminescence spectra for the hexagonal polymorph of $[Au_3(MeN{=}COMe)_3]$ at 298 K. The photograph shows the white emission color rendered upon irradiation with 365 nm irradiation from a hand-held UV lamp. (b; middle panel) Current density−voltage (*JV*) curves for Schottky diodes with device structures: Left, PVK/Ca-Al. Right, ITO/PEDOT:PSS/10% hexagonal $[Au_3(MeN{=}COMe)_3]$:PVK/Ca-Al. Note the dramatic increase in electrical conductivity due to the hole current of the PVK thin film upon p-doping with $[Au_3(MeN{=}COMe)_3]$. (c; bottom panel) *IV* curves for an organic field effect transistor (OFET) in which single needles of the trimer of hexagonal $[Au_3(MeN{=}COMe)_3]$ are the active semiconductor. The field effect shown in the right-side figure clearly indicates that the trimer is a p-type semiconductor.

species, wherein the creation of an exciton allows the charge distribution to rearrange and the lattice motifs react through a stabilizing deformation.[7] If the stabilizing deformation is large, the exciton will be bound to the area of lattice deformation.

Various Au^I complexes exhibit visible photoluminescence with long phosphorescent lifetimes at room temperature.[6] The large (>6000 cm^{-1}) Stokes shift commonly found in such Au^I complexes indicates a metal-centered excimeric emission due to the contraction of the ground-state aurophilic association upon photoexcitation.[2,4] There is a smaller (2778 cm^{-1}) Stokes shift in hexagonal $[Au_3(MeN{=}COMe)_3]$, which thus implies a smaller contraction upon excitation. This is supported by the fact that the intermolecular Au--Au distances are already short (3.346 Å) in the ground state, making their further compression less drastic upon photoexcitation (hence minimizing the Stokes loss) or oxidation in the luminescence or thin-film electrical device experiments (Figure 5).

The preliminary diode and organic field effect transistor device data for the hexagonal $[Au_3(MeN{=}COMe)_3]$ complex are shown in Figure 5b and c, respectively. The current density−voltage curves for Schottky diodes with device structures ITO/PEDOT:PSS/10% hexagonal $[Au_3(MeN{=}$

dx.doi.org/10.1021/ic500808q | *Inorg. Chem.* 2014, 53, 7485−7499

$COMe)_3$]:PVK/Ca−Al are displayed (ITO = indium tin oxide, PEDOT:PSS = poly(3,4-ethylenedioxythiophene)-polystyrenesulfonate, PVK = poly(vinylcarbazole)). There is a dramatic increase in electrical conductivity due to the hole current of the PVK host thin film upon p-doping with $[Au_3(MeN{=}COMe)_3]$ (Figure 5b). On the other hand, an organic field effect transistor in which single needles of the hexagonal $[Au_3(MeN{=}COMe)_3]$ trimer are the active semiconductor has been evaluated (Figure 5c, left). The crystalline needles acted as molecular nanowires, as they have exhibited an unmistakable field effect shown on the right side of Figure 5c, clearly manifesting a p-type semiconducting behavior for this solid trimer. It was not possible to process contiguous thin films of hexagonal $[Au_3(MeN{=}COMe)_3]$ because of the solid material's extremely low glass transition temperature (<50 °C), insufficient solubility, and decomposition upon thermal evaporation attempts. The field effect data were reproduced several times for samples that varied in terms of numbers of needles crossing the two gold electrodes, hence the extent of current generated. However, the current magnitude in the pico−nano ampere range did not allow for quantification of the p-mobility of this material.

The structure of the $[Au_3(MeN{=}CO^nBu)_3]$ complex is similar to that of the ordered stack in hexagonal $[Au_3(MeN{=}COMe)_3]$.[4a] Figure 6a shows that crystalline $[Au_3(MeN{=}CO^nBu)_3]$ exhibits a low-energy excitation extending to the visible region (420 nm) and a high-energy blue emission with no additional emission band in the red region. The near-visible excitation is proposed to be due to short aurophilic interactions found in the closely-packed extended chains, Figure 1. The blue emission of this compound occurs from delocalized excitons (direct band gap emission), and the Stokes shift will consequently be small (~3,000 cm^{-1}) because the trimer chains are already strongly bound in the ground state. Attempts to construct diode and organic field effect transistors (OFET) devices from $[Au_3(MeN{=}CO^nBu)_3]$ were unsuccessful due to its low glass transition and melting temperatures.

The solid-state photoluminescence for $[Au_3(^nBuN{=}COMe)_3]$ is given in Figure 6b and shows a high-energy UV excitation (310 nm) and a low-energy red emission with no emission in the blue-green region. The large Stokes shift (17 681 cm^{-1}) is due to the contraction of the long intermolecular Au--Au distance in the dimer of trimers for this complex. On moving from the ground state to the phosphorescent excited state, a rather significant aurophilic contraction or excited-state distortion occurs in the dimer of trimers and is indicated by the aforementioned 17 681 cm^{-1} colossal Stokes shift. The low-energy red emission is due to the formation of an intermolecular excimer in the dimer-of-trimer molecular unit, and the high-energy excitation is due to an electronic transition between discrete molecular orbitals of the dimer of trimer molecules.

Figure 6c shows that $[Au_3(^nBuN{=}CO^nBu)_3]$ has an excitation at 360 nm and a broad emission that crosses the visible spectrum ranging from 400−650 nm. This complex has a loose extended chain structure where the Au--Au distance is shorter than that found in the dimer of trimers and longer than in the packed extended chains. Therefore, the excitation band is lower in energy versus that for the former structures and higher in energy versus the latter. The emission profile shows two bands, one of which is in the blue region while the other is in the orange region, which is quite similar to the photoluminescence of the hexagonal polymorph of $[Au_3(MeN{=}COMe)_3]$. This situation is intermediate between a molecular and semiconductor band structure. Thus, it is reasonable to assign the dual emission that gives rise to a white luminescence color in Figure 6c as a combination of these two cases; namely, the blue band is due to direct band gap emission, while the orange band is due to low-energy molecule-like self-trapped excitons.

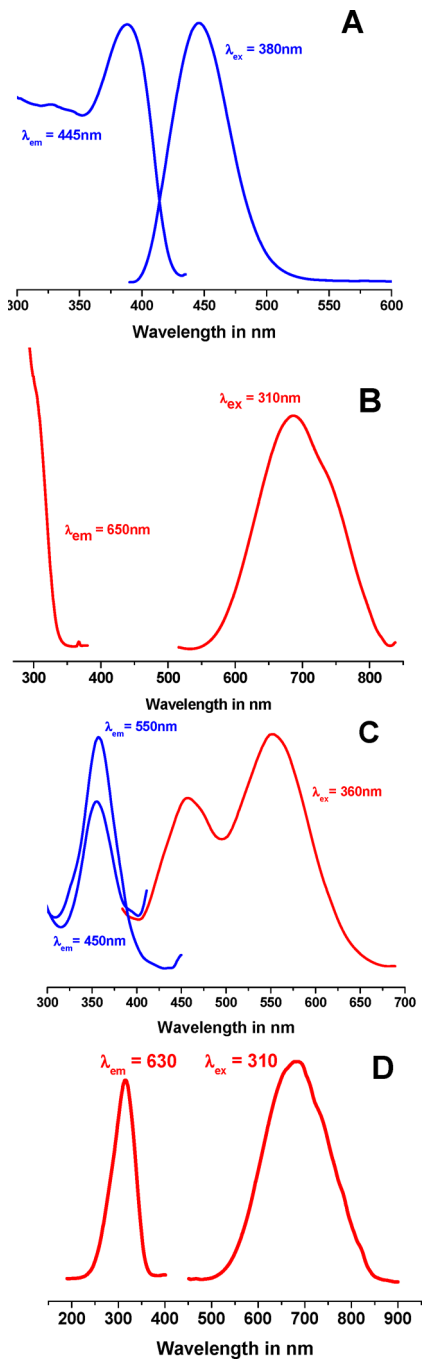

Figure 6. Solid-state photoluminescence spectra at 298 K of (a) $[Au_3(MeN{=}CO^nBu)_3]$, (b) $[Au_3(^nBuN{=}COMe)_3]$, (c) $[Au_3(^nBuN{=}CO^nBu)_3]$, and (d) $[Au_3(^cPeN{=}COMe)_3]$.

Figure 6d shows the luminescence spectra for $[Au_3(^cPeN{=}COMe)_3]$. The complex has a similar crystal structure to that for $[Au_3(^nBuN{=}COMe)_3]$, in which molecules conform to a dimer-of-trimer structure, but with two Au--Au intermolecular interactions between the trimers. A very large Stokes shift of 16

dx.doi.org/10.1021/ic500808q | Inorg. Chem. 2014, 53, 7485−7499

918 cm^{-1} (Table 3) is seen for the $[Au_3(^cPeN{=}COMe)_3]$ solid, consistent with long intermolecular Au--Au distances in

Table 3. Excitation and Emission Maxima (nm) and Stokes Shifts (cm^{-1}) for Trinuclear Gold(I) Complexes

	λ_{ex}^{max}/nm	λ_{em}^{max}/nm	Stokes shift/cm^{-1}
$Au_3(MeN{=}COMe)_3$	400	450	2778
$Au_3(MeN{=}CO^nBu)_3$	388	446	3352
$Au_3(^nBuN{=}COMe)_3$	310	686	17 681
$Au_3(^nBuN{=}CO^nBu)_3$	357	457	6130
$Au_3(^cPeN{=}COMe)_3$	316	679	16 918

the ground state, and more geometric reorganization in the excited state (calculations suggest a drastic contraction of Au--Au intermolecular distances; *vide infra*) for this polymorph, as compared to the extended polymorph I, which has a much smaller (2778 cm^{-1}) Stokes shift. As before, we assign the high-energy excitation to an electronic transition between discrete molecular orbitals of the dimer-of-trimer molecules and the low-energy emission to an intermolecular excimer in a dimer of trimers.

3. Periodic Modeling of Gold Carbeniate Complexes. Preliminary calculations at the extended Hückel tight binding (EHTB) level of theory revealed interesting variations in the total and partial density of states for the trimeric gold carbeniates from the Balch[4] and Omary laboratories, both in the conduction and valence bands (see Supporting Information). Given the interesting variations in crystal symmetry/morphology with variations in R and R′, we sought to use first-principles computations to dissect the experimentally observed solid-state structural variations to quantify their impact upon the condensed phase electronic structure of Au_3Cb_3 complexes and the resulting photophysical and conduction properties.

The structural variations that impact trimer−trimer interactions in the solid state can be divided into three categories: (i) trimer−trimer stacking distance (R), (ii) rotational motion of one trimer relative to the other about the 3-fold axis (Θ); and (iii) lateral motion of one trimer relative to the other (L), Chart 4. Similar structural modifications were investigated in an

Chart 4. Different Structural Variations That Impact Trimer−Trimer Interactions in the Solid State[a]

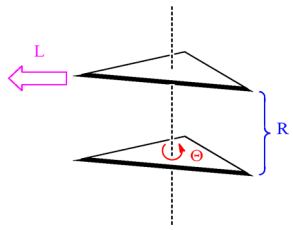

[a]The two triangles represent two Au_3Cb_3 trimers. R, Θ, L indicate intertrimer separation, rotation, and lateral movement, respectively.

earlier contribution from our groups utilizing *molecular* cyclotrimer models and molecular (i.e., Gaussian-based) density functional theory (DFT) calculations. One pertinent conclusion from that previous contribution was that such molecular motions were "soft".[9] Hence, one may propose from such precedents, and from the structural diversity discussed above, that there is substantial potential to design crystal growth of gold carbeniate complexes utilizing aurophilic interactions, hydrogen bonding, and electrostatic interactions. As such, one might expect that it is possible to rationally design complexes with desirable chemical properties and, more importantly, materials with desirable condensed phase and device-level properties. Given such goals, it was deemed prudent to use the same substituents to minimize differences due to the donor/acceptor properties of R and R′. Furthermore, to minimize computational expense, we chose R = R′ = H. Finally, the structural transformations in Chart 4 are evaluated with plane-wave (PW) DFT methods.

To study the effect of the three structural changes depicted in Chart 4 with PW-DFT calculations, crystal structures were built to model each structural change. In the following sections we will discuss how the crystal structures are built for each structural change and how they impact the band gap.

i. Intertrimer Separation (R). Balch's perfectly stacked structure (**I**)[4a] was taken as a template[4b,10] to probe the effect of R (Chart 4) modification along the c-axis of the unit cell. A crystal structure (Supporting Information) with four gold carbeniate trimers in the unit cell (Figure 7) with two pairs

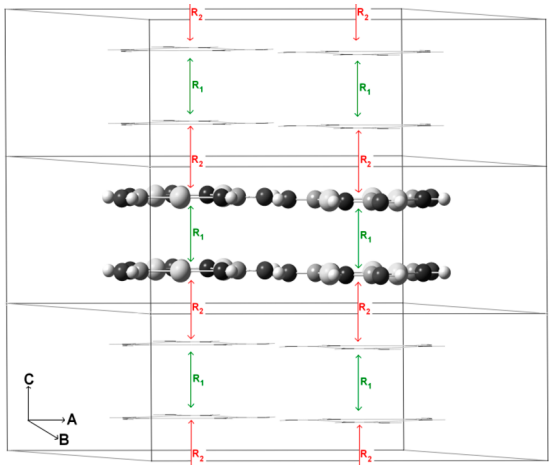

Figure 7. Unit cell with two images (above and below) along the c-axis from the built crystal structure of the hypothetical cyclo-$[Au_3(HN{=}COH)_3]$ complex. R_1 and R_2 represent intertrimer distances within the unit cell and from the image cell, respectively.

each stacking as an eclipsed structure (**I**) inside the unit cell was built as the reference. With this reference structure, the effect of R (intertrimer separation) was studied in two cases:

Case A entails constantly increasing or decreasing R of the eclipsed stack (**I**) within the unit cell and its image (i.e., $R_1 = R_2$ in Figure 7).

Case B entails fixing R_1 of the eclipsed stack (**I**) to the experimental Au--Au bond length, 3.346 Å,[4a] within the unit cell, but changing R_2, and hence the distance of a cyclotrimer with its image cell (i.e., $R_1 \neq R_2$ in Figure 7) along the c-axis of the crystal, which can be made by modifying the unit cell c-axis length while keeping R_1 constant. *Case A* represents an infinite stack with constant intertrimer distances, and *Case B* models asymmetric stacking with irregular intertrimer distances. PW-DFT calculations are performed on both cases to study the effect of R on their band structure.

In *case A* ($R_1 = R_2$), the band gap (BG) is calculated for structures with R in the range 2.346−5.346 Å. From Figure 8, *it can be seen that the band gap increases as the intertrimer distance increases.* At the experimental intertrimer distance[4a] of 3.346 Å,

dx.doi.org/10.1021/ic500808q | Inorg. Chem. 2014, 53, 7485−7499

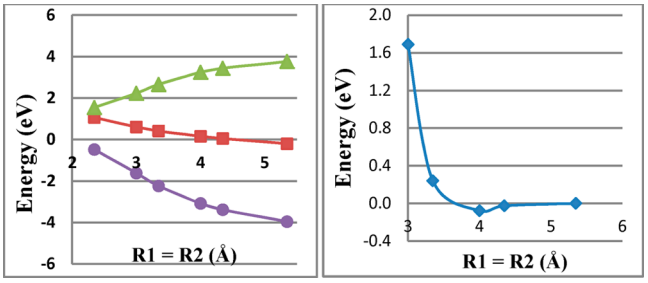

Figure 8. Band structures (left) and relative energies (right) of cyclo-$[Au_3(HN{=}COH)_3]$ complexes with different variations of R mentioned for *case A*. Colors: band gap (green), conduction band (red), valence band (purple), and relative energy (blue).

the calculated BG is 2.65 eV. The drastic drop in BG at $R_1 = R_2 = 2.346$ and at 3.000 Å is caused by band broadening due to very short intertrimer distances, which is also reflected in the relative energies (Figure 8) of all complexes considered in *case A*. Note that the rapid increase in energy (>2 eV) at R_1, $R_2 < 3$ Å (data points of relative energies for $R_1 = R_2 < 3$ Å are not shown in Figure 8, right) is consistent with experimentally observed intertrimer separations in aurophilic cyclo-$[Au(\mu\text{-}L)]_3$ complexes[8] (L = monoanionic bidentate ligands of C−C, C−N, N−N ligation) in the solid state.

In *case B* ($R_1 \neq R_2$), the band gap is calculated for structures with R_2 in the range 2.004−6.004 Å. From Figure 9, it can be

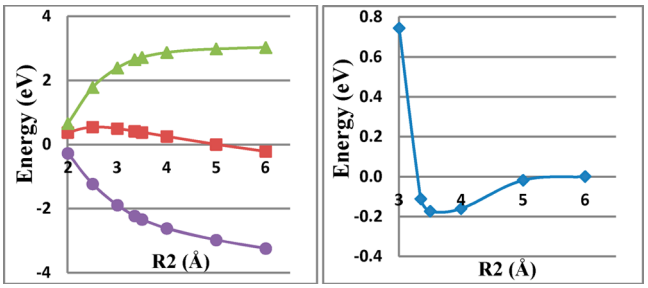

Figure 9. Band structures (left) and relative energies (right) of cyclo-$[Au_3(HN{=}COH)_3]$ complexes with different variantions of R mentioned for *case B*. Colors: band gap (green), conduction band (red), valence band (purple), and relative energy (blue).

seen that the band gap increases with an increase in R_2. *Again, the drastic drop in BG at R_2 = 2.004, 2.504, and 3.004 Å is caused by band broadening due to very short intertrimer distances between neighboring image cells* (Figure 7), which is also reflected in the relative energies (Figure 9, data points of relative energies (>2 eV) for $R_2 < 3$ Å are not shown) of all models considered in *case B*.

Overall, the simulations (both *cases A* and *B*) clearly indicate that shorter intertrimer distances (R_1) with symmetric stacking ($R_1 = R_2$) yield smaller band gaps, suggesting the importance of this structural parameter in making good condensed phase conductors.

ii. Rotational Motion (Θ). Balch's disordered stack (**II**, Chart 2)[4a] is taken as a template[4b,11] to study the effect of Θ (Chart 4) along the *c*-axis of the unit cell. A reference crystal structure (Table S1, Figure S2) was built with four gold carbeniate trimers in the unit cell with two pairs stacking as a staggered structure (**II**) with a rotational angle of 60° inside the unit cell. With this reference structure, the effect of Θ is studied by rotating the trimers from Θ = 60° to 0° in 10° increments.

For all calculations with different Θ values, the unit cell parameters and intertrimer centroid distances (3.346 Å)[4a] are fixed. Band gaps from the PW-DFT calculations with Θ = 0° to 60° are plotted in Figure 10. *The smallest (2.65 eV) and largest*

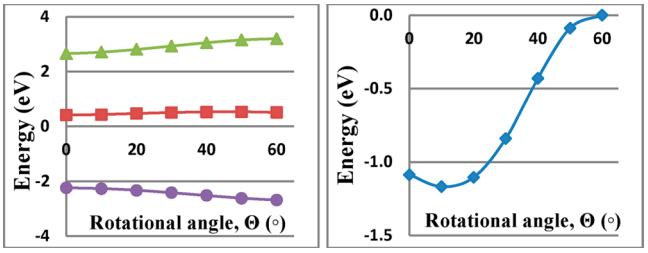

Figure 10. Band structures (left) and relative energies (right) of cyclo-$[Au_3(HN{=}COH)_3]$ complexes with different variantions of Θ. Colors: band gap (green), conduction band (red), valence band (purple), and relative energy (blue).

(3.19 eV) BGs are observed for Θ = 0° and 60°, respectively. Comparing the BG energies, it is obvious that the BG change with Θ is much less than calculated for R changes. However, the relative energy (Figure 10) for the complex with Θ = 0° is 1.09 eV less than for the complex with Θ = 60°. *This indicates that the eclipsed stacks (**I**) are energetically more favorable than staggered stacks (**II**) by ∼1 eV and that this structural transformation serves to reduce the BG.*

iii. Lateral Motion (L). Balch's chair structures (**III**, Chart 2)[4b] are used as templates to study the effect of L (Chart 4). Like in the previous two changes (R, Θ), a crystal structure (Table S1, Figure S3) is built with four gold carbeniate trimers in the unit cell (Figure 11) with two pairs stacking as the chair structure (**III**) with two short Au--Au distances (3.350 Å)[4b] per stack inside the unit cell.

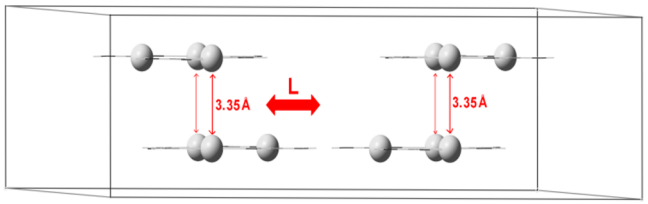

Figure 11. Unit cell from built crystal structure of the Au_3Cb_3 complex to study the variation of lateral movement (L).

The band gap for the chair structure (**III**) with two short Au--Au aurophilic intertrimer bonds (Figure 12) is found to be

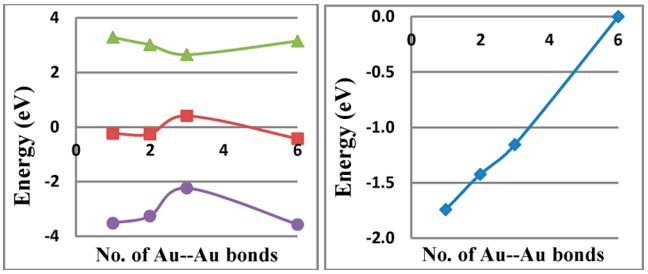

Figure 12. Band structures (left) and relative energies (right) of cyclo-$[Au_3(HN{=}COH)_3]$ complexes with different variantions of L. Colors: band gap (green), conduction band (red), valence band (purple), and relative energy (blue).

dx.doi.org/10.1021/ic500808q | *Inorg. Chem.* 2014, 53, 7485−7499

3.01 eV vs 2.65 eV for the eclipsed stack (**I**) with three short Au--Au distances. With the chair structure (**III**) as reference, the effect of *L* (Chart 4) along the stack is studied by moving the trimers laterally from two short Au--Au aurophilic intertrimer bonds in the stack to six and one Au--Au aurophilic intertrimer bonds, respectively (Table S1, Figure S3). As the trimers move laterally, it is important to note that the distance between the planes of the trimers remains fixed at 3.350 Å.[4b] In the case of the complex with six aurophilic intertrimer Au--Au bonds, the trimers stack in a staggered conformation with Au--Au intertrimer bond lengths of 3.850(±0.030) Å. In the complex with one short Au--Au aurophilic intertrimer bond in the stack, the Au--Au intertrimer bond length is 3.350 Å. Band gaps from PW-DFT calculations of the former and latter geometries are calculated to be 3.28 and 3.15 eV, respectively, i.e., a very small BG difference.

Comparing the band gaps of complexes with 1/2/3/6 short Au--Au aurophilic intertrimer bonds (Figure 12) with fixed interplanar separations indicates that the complex with 3 Au--Au aurophilic intertrimer bonds has smaller band gaps than 1/2/6 Au--Au aurophilic intertrimer bonds (Figure 12). However, the relative energies are found to increase with the increase in the number of Au--Au aurophilic intertrimer bonds (Figure 12) as the two trimers move laterally. *Again, the PW-DFT simulations indicate that eclipsed stacking of trimers is necessary to obtain smaller band gaps in cyclo-[Au$_3$(RN═COR′)$_3$] complexes and that such changes are intimately related to the solid-state morphology.*

4. Molecular Modeling of Gold Carbeniate Complexes. We studied several molecular models of gold carbeniate complexes to evaluate their electronic and excited-state properties. As mentioned earlier, due to the polymorphic nature of cyclo-[Au$_3$(RN═COR′)$_3$] complexes (Charts 1, 2), which likely arise from varying crystal growth conditions and substituents (R, R′), we confined most of the molecular modeling to complexes with R = R′ = H. However, some calculations on complexes with R = Me (methyl) and R′ = Me/^{n}Bu (*n*-butyl) were also performed for comparison, but not detailed in this report, as the conclusions obtained echo those given below for the minimalist molecular models. Molecular calculations with DFT are performed on hypothetical cyclo-[Au$_3$(HN═COH)$_3$] trimer (T) complexes for a monomer of trimer (MOT)/(**VII**), a dimer of trimer (DOT)/(**VIII**/**IX**), and a trimer of trimer (TOT)/(**X**), Figure 13, model. The DOT calculations are performed on both H−H (**V**/**VIII**) and H−T (**VI**/**IX**) conformations (Chart 3), but the TOT calculation is done only on the H−H conformation to conserve computing resources for this large model. It is important to note that DOT and TOT calculations are performed on eclipsed stacks only, given the favorability of this arrangement that emerged from the PW-DFT calculations. Molecular computations on a DOT model for staggered and chair conformations are reported elsewhere[9a] and indicated a soft potential surface with minimal changes in electronic properties. Comparison of MOT, DOT, and TOT complexes will enlighten how dimerization, trimerization, and eventually polymerization of trimers would impact their structural and electronic properties. So, we performed calculations on singlet (S_0) and triplet (T_1) forms of all four models (Figure 13) described above. All structures are completely relaxed without symmetry constraint. Nu (Nu = neutral)/T_1 structures are calculated to determine the spectroscopic and electronic parameters, relative to Nu/S_0 ground states.

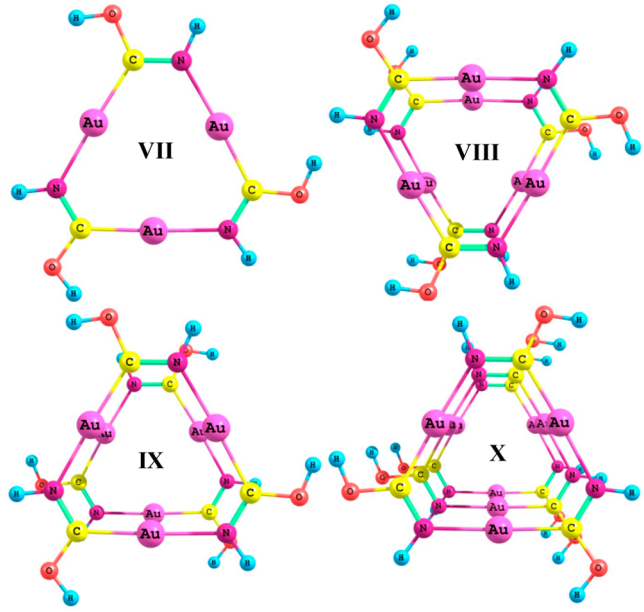

Figure 13. Cyclo-[Au$_3$(HN═COH)$_3$] complexes with different stacking patterns used for molecular modeling. MOT (**VII**), DOT:H−H (**VIII**), DOT:H−T (**IX**), TOT:H−H (**X**).

Geometric Properties. After optimization, all S_0 structures remain more planar than the respective triplets when they stack in DOT and TOT conformations (Figures 14, S5, and S6).

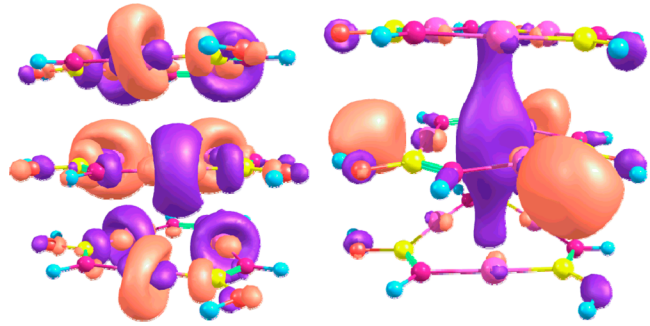

Figure 14. Contours of frontier orbitals of Nu(neutral)/S_0(singlet) TOT complexes. Combined contours of degenerate HOMOs (left) and nondegenerate LUMO (right).

Geometries for S_0 MOT and DOT agree well with experimental geometries.[4a,b] In S_0 TOT complexes, we observe a rotational motion (Θ) of one trimer relative to the other about the 3-fold axis. *Irrespective of the changes in Θ, interestingly, the centroid to centroid distances of adjacent trimers in the stack agree with experiment (vide supra).*[4a,b] The shortest intertrimer Au--Au distances for all DOT and TOT complexes are listed in Table 4. Comparing the intertrimer Au--Au bonds of S_0/T_1 complexes, it is apparent that these bonds in the T_1 states are shorter than in singlets. Also, one Au--Au bond is much shorter than the other two in the stack. This phenomenon is due to the formation of excimeric complexes consistent with cyclo-[M$_3$(μ-Pz)$_3$] (M = Cu/Ag/Au; Pz = pyrazolate) DOT complexes, as reported earlier and discussed above in the experimental section.[3b,9] One other important distinction in comparing S_0 **VIII** and **IX** complexes is that Au--Au bonds are ∼0.15 Å shorter for the latter. This agrees with the crystallographic database analysis in regard to H−T and H−H interactions. We

dx.doi.org/10.1021/ic500808q | Inorg. Chem. 2014, 53, 7485−7499

Table 4. Intertrimer Aurophilic Bonds and Spectroscopic Properties of Cyclo-[$Au_3(HN{=}COH)_3$] Complexes

	intertrimer Au--Au bonds (Å)				
structure	singlet	triplet	excitation $S_0 \rightarrow T_1$ (eV)	emission $T_1 \rightarrow S_0$ (eV)	Stokes shift (eV)
VII (MOT)			4.93	1.44	3.49
VIII (DOT H−H)	3.302, 3.303, 3.306	2.941, 3.068, 3.217	3.80	3.34	0.46
IX (DOT H−T)	3.250, 3.250, 3.262	2.977, 2.977, 3.226	3.72	3.28	0.44
X (TOT H−H)	3.340, 3.340, 3.340	2.978, 3.292, 3.300	3.40	2.87	0.54

propose that this enhancement is due to an enhanced electrostatic interaction (supported by Mulliken and natural population analysis, Figure S9) in the H−T (**IX**) complex vs the H−H (**VIII**) complex, as the intertrimer aurophilic distance and presumably strength of interaction in each complex remain the same for both **VIII** and **IX**. Also, recall from the previous PW-DFT band gap studies reported above that shorter intertrimer distances (R) suggest better conduction behavior for these materials. Hence, we propose that H−T complexes that possess shorter intertrimer Au--Au distances may act as better conductors as compared to H−H materials. The apparent disagreement of this computational finding with the experimental crystal structure of the (Me, ^{n}Bu) head-to-tail complex herein exhibiting slightly longer intertrimer aurophilic contacts vs Balch's hexagonal (Me, Me) head-to-head complex can be attributed to the larger steric factor of the ^{n}Bu vs Me groups and the crystallographic data being at room temperature (296 K) for the former vs low temperature (130 K) for the latter.

Electronic Properties. Frontier orbitals of S_0/T_1 states of d^{10} complexes were reported earlier by many research groups including our own.[3b,9] Contours of frontier orbitals (Figures 14, S5, and S6) for S_0/T_1 states of cyclo-[$Au_3(HN{=}COH)_3$] DOT/TOT (**VIII**, **IX**, **X**) complexes are consistent with previous studies on coinage metal−pyrazolate cyclotrimers.[9] For all optimized DOT/TOT models, there is a doubly degenerate HOMO and a nondegenerate LUMO for the S_0 ground state (Figures S5 and S6). Contours of singly occupied/unoccupied molecular orbitals (SOMO/SUMO) of optimized T_1 states of DOT/TOT complexes indicate the higher energy SOMO of the T_1 states corresponds to the LUMO of the S_0 states, which again is consistent with earlier studies.[3b,9] *The upper SOMO of T_1 and the LUMO of S_0 states show pronounced delocalized, intertrimer bonding across multiple gold centers. They also show increased intertrimer bonding in DOT/TOT complexes.*

Note that the frontier orbitals of the MOT models are slightly different, with both a doubly degenerate HOMO and LUMO for the S_0 ground state (Figure S4). However, the LUMO+1 of the MOT is only 0.023 eV above the LUMO and has delocalized orbitals inside the trimer ring, which yields intertrimer excimer bonding (Figures S4−S6).[9] The frontier orbitals of the S_0 and T_1 states of MOT/DOT/TOT complexes of cyclo-[$Au_3(MeN{=}COMe)_3$] and cyclo-[$Au_3(MeN{=}CO^nBu)_3$] obtained by similar molecular DFT calculations utilizing X-ray (as opposed to DFT-optimized) geometries (not presented in this report) yield similar results in terms of frontier orbital composition, which is predominantly within the metallocycle ring as in cyclo-[$Au_3(HN{=}COH)_3$]. This suggests that the substituents would have minimal influence on the HOMO/SOMO and LUMO/SUMO composition of S_0/T_1 states of gold carbeniate complexes. In addition, note that the morphology of the trimer complexes would be expected to have less effect on the HOMO than the LUMO composition given its disposition. This contention is supported by comparing the HOMO/SOMO and LUMO/SUMO of S_0/T_1 states of eclipsed vs staggered vs chair conformations of MOT/DOT/TOT of cyclo-[$Au_3(HN{=}COH)_3$] complexes (Figures S4−S8).

Spectroscopic Properties. Excitation ($S_0 \rightarrow T_1$) and emission ($T_1 \rightarrow S_0$) energies and Stokes shifts (SS) are calculated on the MOT, DOT, and TOT models (Table 4). It is important to notice that the excitation energies and Stokes shifts typically decrease as the extent of trimer stacking increases, and this agrees with the experimental results (Table 3). The only exception is the SS of TOT, which may be attributed to the increase in the intertrimer Au--Au distances caused by the rotational motion (Θ) of one trimer relative to the other along the 3-fold axis (Figures 14, S6). Nevertheless, the larger SS for the TOT model is consistent with the experimental finding that extended chain structures exhibit less Stokes loss than that for DOT structures; larger models than TOT are needed to attain better correlation with the experimental excitation and emission energies for extended chain structures, however. Also, it was found that these spectroscopic energies decrease for the H−T conformation (**IX**) vs the H−H conformation (**VIII**), which is plausibly due to the augmented electrostatic interaction enhancing intertrimer bonding. This apparent disagreement with the experimental trend (Table 3) is likely due to the use of (H, H) computational dimer-of-trimer models to represent both (Me, ^{n}Bu) head-to-tail and (Me, Me) head-to-head extended-chain experimental structures. The experimental and calculated trend of decreasing Stokes shift energies with an increase in the extent of trimer stacking and decreased intertrimer distances supports the proposal that these Au_3Cb_3 complexes may act as good conducting materials when stacked in the solid state, especially in an H−T conformation.

To distinguish the effect of trimer morphology on their spectroscopic properties, excitation and emission energies of eclipsed (**VIII**, **IX**) and chair (Figure S7) DOT complexes are compared. The excitation/emission/Stokes shift energies of the chair conformer (Figure S7) are found to be 4.04/3.49/0.54 eV, respectively, which are higher than the corresponding energies for the eclipsed conformers by 0.24/0.16/0.08 eV vs model **VIII** and by 0.32/0.21/0.10 eV vs model **IX**, respectively. From this molecular-based comparison, we conclude that eclipsed DOT conformers might be better conductors than the chair given their respective spectroscopic energies, which corroborates the PW-DFT calculations, as the BG for the eclipsed unit cell (H−H conformer **VIII**) is 0.36 eV less than that for the chair unit cell.

Charge Transport Properties. In organic semiconductors, electronic charge transport parameters are dependent on strong coupling between geometric and electronic structures.[12] The degree of chain order (in polymers) and solid-state packing (in crystals) of organic semiconductors are critical for efficient charge transport.[13] At the molecular level, charge transport parameters can be described using the Marcus theory of

dx.doi.org/10.1021/ic500808q | Inorg. Chem. 2014, 53, 7485−7499

Table 5. Charge Transport Properties of Cyclo-[$Au_3(RN{=}COR')_3$] Complexes[a]

complex name	VIP/VEA (eV)	AIP/AEA (eV)	λ-cation (λ^+) (eV)	λ-anion (λ^-) (eV)
cyclo-[$Au_3(HN{=}COH)_3$]	8.377/0.446	8.091/0.285	0.287	0.161
cyclo-[$Au_3(MeN{=}COMe)_3$]	7.724/0.778	7.431/0.407	0.293	0.371
cyclo-[$Au_3(MeN{=}CO^nBu)_3$]	7.486/0.819	7.169/0.441	0.317	0.379

[a]VIP, AIP, VEA, AEA, and λ represent vertical ionization potential, adiabatic ionization potential, vertical electron affinity, adiabatic electron affinity, and reorganization energy, respectively.

electron transfer.[12−14] At high temperatures (room temperature), the electron transfer/hopping rate (k_{et}) can be approximated as[13,15]

$$k_{et} = \frac{4\pi^2}{h}\frac{1}{\sqrt{4\pi\lambda k_b}}t^2 \exp\left(-\frac{\lambda}{4k_bT}\right) \quad (1)$$

Equation 1 is governed by two parameters: the intermolecular transfer integral (t) and the intramolecular reorganization energy (λ). T, k_b, and h represent temperature, Boltzmann's constant, and Planck's constant, respectively. For a more in-depth discussion of the theoretical basis and description of λ and t; see refs 25−28.

In this research, we calculated the intramolecular reorganization energies (λ) of cyclo-[$Au_3(RN{=}COR')_3$] (R = H/Me and R′ = H/Me/^{n}Bu) complexes at both cationic and anionic charged states. Reorganization energies (λ) can be calculated using two methods: the adiabatic potential method and normal-mode analysis.[15a] Herein, we use the adiabatic potential method to determine the reorganization energies. Calculated reorganization energy (λ) values of cyclo-[$Au_3(RN{=}COR')_3$] complexes, for both hole (λ-cation/λ^+) and electron (λ-anion/λ^-) states, are reported in Table 5. We also report molecular adiabatic/vertical ionization potentials (IP) and electron affinities (EA) for the above-mentioned gold carbeniate (Au_3Cb_3) complexes. Vertical ionization potential (VIP) and electron affinity (VEA) represent the IP and EA of Au_3Cb_3 complexes at their neutral geometries; the adiabatic ionization (AIP) and electron affinity (AEA) represent the IP and EA of Au_3Cb_3 complexes at their optimized charged (cation/anion) geometry, Table 5.

Comparison of calculated reorganization energies of cyclo-[$Au_3(RN{=}COR')_3$] (R = H/Me and R′ = H/Me/^{n}Bu) complexes indicates that the λ values for both a hole and an electron increase with the addition of bulky substituents (for R′ = H/Me/^{n}Bu; λ^+ = 0.287/0.293/0.317 and λ^- = 0.161/0.371/0.379 eV, respectively) on the ligands of the gold carbeniate metallocycle. A similar trend is also observed with the VEA and AEA values, Table 5. However, one interesting difference among the three complexes (Table 5) studied here is the VIP and AIP values of cyclo-[$Au_3(HN{=}COH)_3$] (VIP/AIP = 8.38/8.09 eV), which are higher than the other two complexes cyclo-[$Au_3(MeN{=}COMe)_3$] (VIP/AIP = 7.724/7.431 eV) and cyclo-[$Au_3(MeN{=}CO^nBu)_3$] (VIP/AIP = 7.486/7.169 eV). Furthermore, we can observe that for the complex with R′ = H, λ^- (0.161 eV) is lower than its λ^+ (0.287 eV), indicating that reorganization is less for electron transport than hole transpor, for the cyclo-[$Au_3(HN{=}COH)_3$] complex. On the other hand, an opposite trend is observed for complexes with R′ = Me/^{n}Bu (compare λ^+ and λ^- values, Table 5), where reorganization is computed to be greater for electron transport than hole transport. The reason for higher λ^+ values for the cyclo-[$Au_3(HN{=}COH)_3$] complex can be attributed to the increase in the respective VIP (8.377 eV) and AIP (8.091 eV) values.

As mentioned earlier,[12,13b,15] at the microscopic level, along with reorganization energy (λ), the intermolecular transfer integral (t) is an important contributor to determine the electron transfer rate in organic/metal−organic semiconductors. Due to the formation of extended chains (Chart 2, Figure 1) along the c-axis of the unit cell[4] and also due to shorter intermolecular distances of cyclo-[$Au_3(RN{=}COR')_3$] complexes, we anticipate that these complexes have strong electronic couplings (significant transfer integral (t) values) especially along the c-axis and lower effective masses for charge carriers. This prediction is consistent with recent calculations[16] on charge transport properties of [$Au_3(MeN{=}COMe)_3$] crystals. Simulations indicated that [$Au_3(MeN{=}COMe)_3$] has a very small hole effective mass ($0.21m_0$) along the stacking directions of the gold triangles (**I**). Also in the stacking direction, the effective mass of the electron is comparable to pentacene[16] (an organic molecular semiconductor with the highest known charge-carrier mobilities) and should allow efficient electron transport. It was also reported[16] that the electron transport in [$Au_3(MeN{=}COMe)_3$] crystals is isotropic (three-dimensional), while holes are confined to the one-dimensional transport pathway. Hence similar gold(I) cyclotrimer compounds would be a promising ambipolar transport material in electronic devices. Future studies are planned in this direction to obtain a comprehensive picture of charge transport properties of different gold(I) cyclotrimers to guide ongoing synthesis and device work.

SUMMARY AND CONCLUSIONS

A combined experimental and computational study on a diverse series of cyclo-[$Au_3(RN{=}COR')_3$] complexes (R and R′ are a selection of substituents) has been performed. Experimental studies include synthesis, structural characterization, X-ray structure, and photophysical characterization of selected known and novel gold(I) carbeniate complexes **I**−**VIII**.

Inspection of the X-ray crystal structures for the cyclo-[$Au_3(RN{=}COR')_3$] complexes synthesized here and those found in the literature[4−6] indicated that gold(I) carbeniate complexes form polymorphic structures that vary with the ligand substituents (R, R′). Photoluminescence studies show that the polymorphs exhibit distinct spectroscopic properties correlated to the number of aurophilic bonds (1, 2, or 3) and to the Au--Au bond distances in their crystal geometries. Among a variety of [$Au_3(RN{=}COR')_3$] polymorphic structures synthesized by the Balch and Omary groups, it was determined that only two infinitely extended chain structures, [$Au_3(MeN{=}COMe)_3$] and [$Au_3(MeN{=}CO^nBu)_3$], have significantly smaller (~3000 cm^{-1}) Stokes shifts and shorter Au--Au bond distances. Structural properties such as these are desirable toward novel materials applications, in order to produce suitable photophysical and conduction properties for molecular electronic devices. An interesting structural disparity between these two extended stacking complexes, [$Au_3(MeN{=}COMe)_3$] and [$Au_3(MeN{=}CO^nBu)_3$], is that they stack in

dx.doi.org/10.1021/ic500808q | Inorg. Chem. 2014, 53, 7485−7499

the head to head (H−H) and head to tail (H−T) conformations, respectively (Chart 3). This orientation is due to the asymmetric, μ-N,C nature of the bidentate carbeniate ligand.

Due to the differences in the spectroscopic properties of $[Au_3(RN{=}COR')_3]$ complexes bearing numerous polymorphic structures reported from present and earlier[4−6] experiments, a comprehensive computational study of diverse structural forms for the Au_3Cb_3 complexes under both molecular and periodic regimes has been completed. The goal of the computational modeling is to seek the structure−property relationship between the geometric stacking of different polymorphic $[Au_3(RN{=}COR')_3]$ complexes and their respective optoelectronic and conduction properties. Periodic and molecular simulations were performed on all known stacking patterns (Chart 2) of Au_3Cb_3 complexes.

Examination of band gaps and relative energies (Figures 7−12) obtained from periodic simulations of constructed (*vide supra*) polymorphs of $[Au_3(HN{=}COH)_3]$ complexes indicated that shorter intertrimer distances (R) with an eclipsed structure ($\Theta = 0°$) and three Au--Au bonds (L) are essential to obtain better conducting properties pertaining to smaller band gaps with stable geometries. These results were further supported by spectroscopic, electronic, and geometric properties (Figures 13, 14, and S4−S8) obtained from fully optimized molecular geometries of Au_3Cb_3 complexes. Furthermore, molecular computations on H−H and H−T models (Chart 3, Figure 13) indicated that spectroscopic energies decrease for the latter, due to the augmented electrostatic interaction enhancing intertrimer bonding.

Both periodic and molecular simulations on constructed models of $[Au_3(HN{=}COH)_3]$ complexes indicated that the infinitely extended chain of eclipsed head to tail (H−T) structures with equidistant Au--Au aurophilic bonding can have lower band gaps and smaller Stokes shifts and reorganization energies (λ). These simulations predict that if such an extended chain of $[Au_3(RN{=}COR')_3]$ complexes with nonbulky substituents were to be synthesized, they may act as ideal semiconducting materials for molecular electronic devices. OFET devices were constructed using $[Au_3(MeN{=}COMe)_3]$, and a p-type field effect was measured. Hole transport was also increased by 3 orders of magnitude for $[Au_3(MeN{=}COMe)_3]$-doped poly(9-vinylcarbazole). As such, this article reports an important step forward in the rational design of molecular electronic devices via establishment of links between both molecular and solid-state electronic structure and device properties. However, it is also important to note that the device performance is dependent not only on the properties of the semiconducting material alone but also on its interface characteristics with other device components. Research toward this goal is now under way in our laboratories.

EXPERIMENTAL METHODS

A. Synthetic and Photophysical Studies. All reactions were carried out under an argon atmosphere. The solvents used were distilled from conventional drying agents, degassed prior to use, and stored under argon. The *n*-butyl isocyanide and cyclopentyl isocyanide were purchased from Acros Organics. The methyl isocyanide,[30] chloro(tetrahydrothiophine)gold(I),[31] and chloro-(triphenylphosphine)gold(I)[31] were prepared as published. ^{1}H and ^{13}C NMR spectra were recorded in deuterated solutions on a Varian 500 MHz NMR instrument at 500 MHz. Chemical shifts are reported as δ in units of parts per million (ppm). The following abbreviations were used: s, singlet; d, doublet; t, triplet; m, multiplet. Infrared spectra were recorded in the range 300−4000 cm^{-1} on a PerkinElmer Spectrum One FT-IR spectrophotometer using pressed potassium bromide pellets.

I *$[Au_3(MeN{=}COMe)_3]$.* A published procedure was used for the synthesis of $[Au_3(MeN{=}COMe)_3]$.[32] The evaporation of a dichloromethane solution of the complex yielded a colorless microcrystalline powder.

V *$[Au_3(MeN{=}CO^nBu)_3]$.* A solution of 0.044 g (0.780 mmol) of potassium hydroxide and 0.042 mL (0.780 mmol) of methyl isocyanide was dissolved in 20 mL of *n*-butyl alcohol. The solution was stirred in an ice bath for 0.5 h. The slow addition of 0.250 g (0.780 mmol) of chloro(tetrahydrothiophene)gold(I) caused the solid to dissolve. The solution was stirred for 1 h, before the solvent was removed under vacuum. The crude material was dissolved in dichloromethane, and the solution was filtered through Celite. The solvent was removed, leaving a white solid; 10 mL of methanol was added to dissolve the solid, and the solution was cooled in a liquid nitrogen bath until a white precipitate formed. The solid was filtered and washed with cold ether. Purification was accomplished by the recrystallization from a liquid nitrogen cooled solution of methanol; mp 79−80 °C, yield 62%. IR spectrum: ν(C=N) 1576 cm^{-1}. ^{1}H NMR (δ in $CDCl_3$): 4.401 ppm, t, −O−CH_2; 2.883 ppm, m, −O−CH_2−CH_2; 1.681 ppm, m, −O−CH_2−CH_2−CH_2; 1.379 ppm, m, −O−CH_2−CH_2−CH_2−CH_3; 0.924 ppm, s, −N−CH_3. ^{13}C NMR (δ in $CDCl_3$): 199.183 ppm, −Au−C=N−; 72.236 ppm, −O−CH_2; 39.244 ppm, −O−CH_2−CH_2; 18.744 ppm, −O−CH_2−CH_2−CH_2; 13.703 ppm, −O−CH_2−CH_2−CH_2−CH_3; 31.808 ppm, −N−CH_3.

VI *$[Au_3(^nBuN{=}COMe)_3]$.* A solution of 0.044 g (0.780 mmol) of potassium hydroxide and 0.082 mL (0.780 mmol) of *n*-butyl isocyanide was dissolved in 20 mL of methanol. The solution was stirred in an ice bath for 0.5 h. The slow addition of 0.250 g (0.780 mmol) of chloro(tetrahydrothiophene)gold(I) caused the solid to dissolve and was quickly followed by the precipitation of a white solid. After the mixture was stirred for 1 h, the solid was filtered and washed with cold ether. Purification was accomplished by the recrystallization from dichloromethane−ether; mp 74−75 °C, yield 56%. IR spectrum: ν(C=N) 1547 cm^{-1}. ^{1}H NMR (δ in $CDCl_3$): 3.997 ppm, s, −O−CH_3; 3.412 ppm, m, −N−CH_2; 1.962 ppm, m, −N−CH_2−CH_2; 1.369 ppm, m, −N−CH_2−CH_2−CH_2; 0.891 ppm, t, −N−CH_2−CH_2−CH_2−CH_3. ^{13}C NMR (δ in $CDCl_3$): 199.688 ppm, −Au−C=N−; 59.144 ppm, −O−CH_3; 48.891 ppm, −N−CH_2; 33.280 ppm, −N−CH_2−CH_2; 20.303 ppm, −N−CH_2−CH_2−CH_2; 13.941 ppm, −N−CH_2−CH_2−CH_2−CH_3.

VII *$[Au_3(^nBuN{=}CO^nBu)_3]$.* A solution of 0.044 g (0.780 mmol) of potassium hydroxide and 0.082 mL (0.780 mmol) of *n*-butyl isocyanide was dissolved in 20 mL of *n*-butyl alcohol. The solution was stirred in an ice bath for 0.5 h. The slow addition of 0.250 g (0.780 mmol) of chloro(tetrahydrothiophene)gold(I) caused the solid to dissolve. After the solution was stirred for 1 h, the solvent was removed under vacuum. The crude material was dissolved in dichloromethane, and the solution was filtered through Celite. The solvent was removed, leaving a white solid. A 10 mL amount of methanol was added to dissolve the solid, and the solution was cooled in a liquid nitrogen bath until a white precipitate formed. The solid was filtered and washed with cold ether. Purification was accomplished by the recrystallization from a liquid nitrogen cooled solution of methanol. IR spectrum: ν(C=N) 1528 cm^{-1}. ^{1}H NMR (δ in $CDCl_3$): 4.408 ppm, t, −O−CH_2; 1.666 ppm, m, −O−CH_2−CH_2; 1.373 ppm, m, −O−CH_2−CH_2−CH_2; 0.921 ppm, m, −O−CH_2−CH_2−CH_2−CH_3; 3.395 ppm, m, −N−CH_2; 1.666 ppm, m, −N−CH_2−CH_2; 1.373 ppm, m, −N−CH_2−CH_2−CH_2; 0.921 ppm, t, −N−CH_2−CH_2−CH_2−CH_3. ^{13}C NMR (δ in $CDCl_3$): 198.655 ppm, −Au−C=N−; 71.772 ppm, −O−CH_2; 32.172 ppm, −O−CH_2−CH_2; 18.986 ppm, −O−CH_2−CH_2−CH_2; 13.837, −O−CH_2−CH_2−CH_2−CH_3; 49.092 ppm, −N−CH_3, −N−CH_2; 33.258 ppm, −N−CH_2−CH_2; 20.303 ppm, −N−CH_2−CH_2−CH_2; 13.956 ppm, −N−CH_2−CH_2−CH_2−CH_3.

VIII *$[Au_3(^cPeN{=}COMe)_3]$.* A solution of 0.044 g (0.780 mmol) of potassium hydroxide and 0.083 mL (0.780 mmol) of cyclopentyl isocyanide was dissolved in 20 mL of methanol. The solution was

dx.doi.org/10.1021/ic500808q | Inorg. Chem. 2014, 53, 7485−7499

stirred and cooled in an ice bath. The slow addition of 0.250 g (0.780 mmol) of tetrahydrothiophene gold(I)chloride, Au(THT)Cl, caused the solid to dissolve, but was quickly followed by the precipitation of a colorless solid. After the mixture was stirred for 1 h, the solid was collected by filtration and washed with ether. Purification was accomplished by recrystallization from dichloromethane−ether; mp 189−190 °C, yield 52%. ^{1}H NMR (δ in $CDCl_3$): 3.978 ppm, s, −O−CH_3; 1.874 ppm, m, −N−CH; 1.715 ppm, m, −N−CH$(CH_2)_2$; 1.525 ppm, m, −N−CH$(CH_2)_2(CH_2)_2$. ^{13}C NMR (δ in $CDCl_3$): 199.2 ppm, −Au-C═N−; 59.1 ppm, −O−CH_3; 57.4, 34.8, 24.5 ppm, −C_5H_7.

Crystals suitable for X-ray structure determinations were obtained by the slow evaporation of a 20 mg sample of the complex dissolved in 3 mL of dichloromethane. After several days small colorless needle crystals formed and were isolated in nearly quantitative yield.

Structure Determination of ***V, VI, VII, and VIII*** *by X-ray Crystallography.* Crystal structure determination for compounds **V**−**VIII** was carried out using a Bruker SMATR APEX2 CCD-based X-ray diffractometer equipped with a low-temperature device and Mo-target X-ray tube (wavelength = 0.71073 Å). For the complex **V** measurements were taken at 296(2) K (crystals fall apart at any low temperature), and for **VI**−**VIII** at 100(2) K. Data collection, indexing, and initial cell refinements were carried out using APEX2;[33] frame integration and final cell refinements were done using SAINT.[34] An absorption correction was applied using the program SADABS.[35] All non-hydrogen atoms were refined anisotropically. The hydrogen atoms in the compounds **V**−**VIII** were placed in idealized positions and were refined as riding atoms. Structure solution, refinement, graphics generation, and generation of publication materials were performed by using SHELXTL software.[36] It should be noted that the X-ray data for the $[Au_3(MeN{=}CO^nBu)_3]$ compound were collected at room temperature, and ^{n}Bu substituents are highly disordered. Under such conditions, non-hydrogen atoms have high U_{eq} (especially terminal C atoms) and connecting hydrogens have a large U_{iso} (U_{eq} = equivalent isotropic displacement and U_{iso} = isotropic displacement). As a consequence CheckCIF/PLATON tests give several A and B alerts about it and low C−C bond precision. All attempts to get experimental data at low temperature for compound **V** failed as noted above.

Photophysical Properties of ***V, VI, VII, and VIII*** *by Photoluminescence.* The luminescence measurements were carried out for purified recrystallized material. Steady-state luminescence spectra were acquired with a Photon Technology International (PTI) Quanta-Master model QM-4 scanning spectrofluorometer. The excitation and emission spectra were corrected for the wavelength-dependent lamp intensity and detector response, respectively.

B. Device Fabrication and Testing. Schottky diode devices employed glass/ITO substrates, which were cleaned by sonication in a sequential series of solvents, including acetone, 2-propanol, and deionized water. The substrates were dried with flowing nitrogen after cleaning and then were treated with oxygen plasma (PLASMALINE 415) for 10 min. The ITO substrate and all organic molecules besides the cyclotrimers (organic solvents and the polymer host poly-*N*-vinylcarbazole) were purchased from H. W. Sands, Sigma-Aldrich, and Lumtec Ltd./Taiwan. The OFET devices were fabricated on Si (100) substrates with a 500 nm layer of thermally grown SiO_2 for isolation. The (80 nm) chromium (Cr) gate metal was deposited using e-beam evaporation. S1813 photoresist (Microchem) was spin-coated at 1500 rpm with a ramp rate of 3000 rpm/s for 60 s and baked at 115 °C for 2 min. These deposition conditions yield a thickness of approximately 1.5 μm. The wafer was exposed to UV light (Karl Suss MA6B contact printer) with a dose of 130 mJ/cm^2 and developed (Microchem, MF319) for 55 s. The sample was rinsed with deionized (DI) water, blown dry with nitrogen, and baked in an oven for 5 min at 95 °C. The Cr layer was wet etched with chromium etchant (CR-7, Cyantek Inc.), rinsed with DI water, and blown dry with nitrogen. The photoresist was removed with acetone followed by isopropyl alcohol, and the substrate was baked at 95 °C for 5 min. The parylene-C (500 nm) ILD layer was deposited using chemical vapor depositions. The next step was to pattern the parylene ILD layer. S1813 photoresist (Microchem) was spin-coated (1500 rpm, 3000 rpm/s, 60 s, 1.5 μm) and baked at 85 °C for 10 min. The wafer was exposed (Karl Suss MA6B contact printer) with a dose of 130 mJ/cm^2 and developed (Microchem, MF319) for 55 s. The sample was rinsed with DI water, blown dry with nitrogen, and baked in an oven for 5 min at 95 °C. An O_2 reactive ion etch (RIE, Technics 85-RIE) (100 mTorr, 50 W, 100 nm/min) was used to etch the parylene interlayer dielectric (ILD) layer, opening the active channel area and gate contact pad. The photoresist was removed with a double-exposure technique by exposing the remaining resist (Karl Suss MA6B contact printer) to a dose of 130 mJ/cm^2 and developed (Microchem, MF319) for 55 s. The wafer was then baked at 95 °C for 10 min. The low-temperature photolithography process and double-exposure technique were used to define the remaining OFET layers. Parylene-C (150 nm) was deposited to form the gate dielectric layer. O_2 RIE (100 mTorr, 50 W, 100 nm/min) was used to pattern the parylene dielectric layer. Au (100 nm) was deposited using e-beam evaporation at 0.5 nm/min for the S−D contacts. Finally, the organic semiconductor was deposited, encapsulated with parylene, and patterned. Organic semiconductor deposition was attempted by spin-coating of the hexagonal $[Au_3(MeN{=}COMe)_3]$ complex from dichloromethane. While multiple attempts were made to attain a contiguous thin film by varying the concentration, temperature, and/or spinning rate, all these attempts resulted in crystallization of the material to form thin needles, some of which were as long as 10 μm (i.e., longer than the ∼5.5 μm horizontal distance between the source and drain gold electrodes). Such longer needles that were randomly oriented to cross the two gold contacts gave rise to the observed field effect.

Thermal evaporation of the organic materials and metals was performed using Knudsen cells in a high-vacuum chamber from Cooke Vacuum with a base pressure below 8 × 10^{-7} Torr (1 Torr = 133.322 Pa). The chamber was vented to load and align the shadow masks for cathode deposition. Quartz crystal oscillators were used to monitor the film thicknesses, which were calibrated *ex situ* using a profilometer (VEECO DEKTAK VIII). The active area of all devices is 10 mm^2. A calibrated spectrophotometer, PR-650 (PhotoResearch, Inc.), was used to measure the electroluminescence spectrum of the Schottky diode devices; however, no light emission was detectable. A Keithley 2400 source-meter unit linked to a calibrated silicon photodiode, controlled by a LabView interface, was used for the measurement of current−voltage characteristics of all Schottky diode and OFET devices. All electrical measurements were carried out in air at room temperature.

■ COMPUTATIONAL METHODS

A. Solid-State Modeling Methods. Solid-state calculations are carried out using the VASP (Vienna *ab Initio* Simulation Program) code.[17,18] Density functional theory within the PAW (projector-augmented Wave) method,[19] and generalized gradient approximation (GGA) functional of Perdew, Burke, and Ernzerhof[20] was employed. Electronic wave functions are sampled on a 1 × 1 × 3 *k*-mesh in the irreducible Brillouin zone using the Monkhorst−Pack method.[21] The cutoff energy of the wave functions was 400 eV. Convergence of total energy with the *k*-mesh in the Brillouin zones and the plane wave cutoff energy was checked. Gaussian smearing was used to set the partial occupancies for each wave function with a smearing width of 0.05 eV.

B. Molecular Modeling Methods. The Gaussian 09 package is used to perform density functional calculations on molecular entities.[22] Los Alamos valence basis sets, LANL2DZ(2f,p)*[23,24] (with augmented d-polarization functions taken from the 6-31G* basis set on main group elements), are employed in conjunction with the M06 functional[25] for all optimization and single-point calculations. The LANL2DZ(2f,p)* basis set[24] was chosen as per an earlier study by Barakat et al. involving Au complexes, where an extended basis set was used, particularly on the gold atoms augmented by two f functions[26] and one Couty−Hall outer p function.[27] Calculations with the M06 functionals gave results more consistent with available experimental data and even outperformed B3LYP functional[28] and higher order, wave function-based MP2[29] calculations. Indeed, the latter, if anything, yields an overly bound Au_3Cb_3 dimer of trimers (intertrimer

dx.doi.org/10.1021/ic500808q | Inorg. Chem. 2014, 53, 7485−7499

separations ~2.8 Å). Hence, we focused our attention on the newer, hybrid meta-GGA functional of Truhlar and co-workers.[25] All geometries are optimized with restricted Kohn–Sham methods for singlet spin states and unrestricted Kohn–Sham methods for triplet multiplicities.

■ ASSOCIATED CONTENT

Ⓢ Supporting Information

This material is available free of charge via the Internet at http://pubs.acs.org.

■ AUTHOR INFORMATION

Corresponding Authors

*E-mail: omary@unt.edu (M. A. Omary).
*E-mail: t@unt.edu (T. R. Cundari).
*E-mail: gnade@utdallas.edu (B. E. Gnade).

Notes

The authors declare no competing financial interest.

■ ACKNOWLEDGMENTS

The authors dedicate this paper to the memory of Prof. Oussama El-Bjeirami, who was a vital part of this research team and a special friend to the authors. M.A.O., T.R.C., and B.E.G. thank the National Science Foundation (CHE-0911690) and the Texas Higher Education Board's Norman Hackerman Advanced Research Program (009741-0089-2007) for support. Calculations employed the University of North Texas (UNT) computational chemistry resource, supported by the NSF through grant CHE-0741936. Partial support by the Welch Foundation (Grant B-1542 to M.A.O.) and NSF (Grant CHE-0701247 to T.R.C.) is also acknowledged. This research was also supported in part by a grant of supercomputer time to T.R.C. by the National Science Foundation through TeraGrid resources provided by the NCSA. H.R. acknowledges the UNT Department of Chemistry and the Moroccan government for travel support and the CASCaM facility for computing resources. X.W. acknowledges support by the U.S. Department of Energy, Office of Science, under Contract No. DE-AC05-00OR22725 managed by UT Battelle, LLC.

■ REFERENCES

(1) (a) Cotton, F. A.; Wilkinson, G.; Murrillo, C. A.; Bochmann, M. In *Advanced Inorganic Chemistry*; Wiley-Interscience: New York, 1999; Chapter 18. (b) Shriver, D. F.; Kaesz, H. D.; Adams, R. D. *The Chemistry of Metal Clusters Complexes*; VCH Publishers, Inc.: New York. 1990. (c) Yang, X.; Zheng, Z.; Knobler, C. B.; Hawthorne, M. F. *J. Am. Chem. Soc.* **1993**, *115*, 193–195. (d) Ehlert, M. K.; Rettig, S. J.; Storr, A.; Thompson, R. C.; Trotter, J. *Can. J. Chem.* **1990**, *68*, 1444–1449. (e) Raptis, R. G.; Fackler, J. P. *Inorg. Chem.* **1988**, *27*, 4179–4182. (f) Sartori, P.; Golloch, A. *Chem. Ber.* **1968**, *101*, 2004–2009. (g) Cundari, T. R.; Chilukuri, B.; Hudson, J. M.; Minot, C.; Omary, M. A.; Rabaâ, H. *Organometallics* **2010**, *29*, 795–800.

(2) (a) Dias, H. V. R.; Diyabalanage, H. V. K.; Eldabaja, M. G.; Elbjeirami, O.; Rawashdeh-Omary, M. A.; Omary, M. A. *J. Am. Chem. Soc.* **2005**, *127*, 7489–7501. (b) Omary, M. A.; Rawashdeh-Omary, M.; Gonser, M. W. A.; Elbjeirami, O.; Grimes, T.; Cundari, T. R.; Diyabalanage, H. V. K.; Gamage, C. S. P.; Dias, H. V. R. *Inorg. Chem.* **2005**, *44*, 8200–8210. (c) Yang, C.; Messerschmidt, M.; Coppens, P.; Omary, M. A. *Inorg. Chem.* **2006**, *45*, 6592–6594. (d) Rawashdeh-Omary, M. A.; Rashdan, M. D.; Dharanipathi, S.; Elbjeirami, O.; Ramesh, P.; Dias, H. V. R. *Chem. Commun.* **2011**, *47*, 1160–1162. (e) Elbjeirami, O.; Rawashdeh-Omary, M. A.; Omary, M. A. *Res. Chem. Intermed.* **2011**, *37*, 691–703. (f) Forward, J. M.; Fackler, J. P., Jr.; Assefa, Z. Photophysical and Photochemical Properties of Gold(I) Complexes. In *Optoelectronic Properties of Inorganic Compounds*; Roundhill, D. M.; Fackler, J. P., Jr., Eds.; Plenum: New York, 1999, Chapter 6. (g) Omary, M. A.; Mohamed, A. A.; Rawashdeh-Omary, M. A.; Fackler, J. P., Jr. *Coord. Chem. Rev.* **2005**, *249*, 1372–1381. (h) Tang, M. C.; Tsang, D. P. K.; Chan, M. M. Y.; Wong, K. M. C.; Yam, V. W. W. *Angew. Chem.* **2013**, *125*, 464; *Angew. Chem., Int. Ed.* **2013**, *52*, 446. (i) Fianchini, M.; Campana, C. F.; Chilukuri, B.; Cundari, T. R.; Petricek, V.; Dias, H. V. R. *Organometallics* **2013**, *32*, 3034–3041. (j) Lintang, H. O.; Kinbara, K.; Yamashita, T.; Aida, T. *Chem.—Asian J.* **2012**, *7*, 2068–2072. (k) Yang, G.; Raptis, R. G. *Angew. Chem., Int. Ed.* **2003**, *42*, 261–263.

(3) (a) Pyykkö, P. *Chem. Rev.* **1997**, *97*, 597–636. (b) Pyykkö, P. *Angew. Chem., Int. Ed.* **2004**, *43*, 4412–4456. (c) Pyykkö, P. *Inorg. Chim. Acta* **2005**, *358*, 4113–4130. (c) Mendizabal, F.; Reyes, D.; Olea-Azar, C. *Int. J. Quantum Chem.* **2006**, *106* (4), 906–912. (d) Mendizabal, F.; Salazar, R. *J. Mol. Model.* **2013**, *19*, 1973–1979. (e) Rodríguez-Castillo, M.; Monge, M.; López-de-Luzuriaga, J. M.; Elena Olmos, M.; Laguna, A.; Mendizabal, F. *Comp. Theor. Chem.* **2011**, *965*, 163–167. (f) Burgos, D.; Olea-Azar, C.; Mendizabal, F. *J. Mol. Model.* **2012**, *18*, 2021–2029.

(4) (a) Vickery, J. C.; Olmstead, M. M.; Fung, E. Y.; Balch, A. L. *Angew. Chem., Int. Ed.* **1997**, *36*, 1179–1181. (b) White-Morris, R.; Olmstead, M. M.; Attar, S.; Balch, A. L. *Inorg. Chem.* **2005**, *44*, 5021–5029. (c) Winkler, K.; Wysocka-Zolopa, M.; Recko, K.; Dobrzynski, L.; Vickery, J. C.; Balch, A. L. *Inorg. Chem.* **2009**, *48*, 1551–1558. (d) Ni, W.; Li, M.; Zheng, J.; Qiu, Y.; Ng, S. W.; Li, D. *Angew. Chem., Int. Ed.* **2013**, *52*, 13472–13476.

(5) (a) Schmidbaur, H.; Graf, W.; Müller, G. *Angew. Chem., Int. Ed. Engl.* **1988**, *27*, 417–419. (b) Harwell, D. E.; Mortimer, M. D.; Knobler, C. B.; Anet, F. A. L. *J. Am. Chem. Soc.* **1996**, *118*, 2679–2685. (c) Vickery, J. C.; Balch, A. L. *Inorg. Chem.* **1997**, *36*, 5978–5983. (d) Schmidbaur, H. *Nature.* **2001**, *413*, 31–33. (e) Panthanemi, S. S.; Desiraju, G. R. *J. Chem. Soc., Dalton Trans.* **1993**, 319–322. (f) Schmidbaur, H.; Schier, A. *Chem. Soc. Rev.* **2012**, *41*, 370–412.

(6) (a) Olmstead, M. M.; Jiang, F.; Attar, S.; Balch, A. L. *J. Am. Chem. Soc.* **2001**, *123*, 3260–3267. (b) Fung, E. Y.; Olmstead, M. M.; Vickery, J. C.; Balch, A. L. *Coord. Chem. Rev.* **1998**, *171*, 151–159.

(7) (a) Gliemann, G.; Holzapfel, W.; Yersin, H. *J. Phys. (Fr.)* **1985**, *46* (Suppl. C), 7–129. (b) Gliemann, G.; Yersin, H. *Struct. Bonding (Berlin, Ger.)* **1985**, *62*, 87. (c) Yersin, H.; Gliemann, G. *Ann. N.Y. Acad. Sci.* **1978**, *313*, 539.

(8) Allen, F. *Acta Crystallogr.* **2002**, *58*, 380–388.

(9) (a) Grimes, T.; Omary, M. A.; Dias, H. V. R.; Cundari, T. R. *J. Phys. Chem. A* **2006**, *110*, 5823–5830. (b) Chilukuri, B.; Cundari, T. R. *J. Phys. Chem. C* **2011**, *115*, 5997–6003. (c) Chilukuri, B.; Cundari, T. R. *Surf. Sci.* **2012**, *606*, 1100–1107.

(10) Bartolomé, C.; Carrasco-Rando, M.; Coco, S.; Cardovilla, C.; Espinet, P.; Martín-Alvarez, J. M. *Organometallics* **2006**, *25*, 2700–2703.

(11) Tiripicchio, A.; Camellini, M. T.; Minghetti, G. *J. Organomet. Chem.* **1979**, *171*, 399–406.

(12) (a) Bao, G.; Locklin, J. In *Organic Field-Effect Transistors*; CRC Press: Boca Raton, 2007; Section 1.1. (b) Brédas, J. L.; Beljonne, D.; Coropceanu, V.; Cornil, J. *Chem. Rev.* **2004**, *104*, 4971–5003.

(13) (a) Cornil, J.; Calbert, J. P.; Brédas, J. L. *J. Am. Chem. Soc.* **2001**, *123*, 1250–1251. (b) Brédas, J. L.; Cornil, J.; da, D. A.; Filho, S. *Proc. Natl. Acad. Sci. U.S.A.* **2002**, *99*, 5804–5809. (c) Cornil, J.; Beljonne, D.; Calbert, J. P.; Brédas, J. L. *Adv. Mater.* **2001**, *13*, 1053–1067. (d) Mas-Torrent, M.; Hadley, P.; Bromley, S. T.; Ribas, X.; Tarrés, J.; Mas, M.; Molins, E.; Veciana, J.; Rovira, C. *J. Am. Chem. Soc.* **2004**, *126*, 8546–8553. (e) Bromley, S. T.; Mas-Torrent, M.; Hadley, P.; Rovira, C. *J. Am. Chem. Soc.* **2004**, *126*, 6544–6545.

(14) (a) Marcus, R. A. *Rev. Mod. Phys.* **1993**, *65*, 599–610. (b) Marcus, R. A. *J. Chem. Phys.* **1956**, *24*, 966–988. (c) Marcus, R. A.; Sutin, N. *Biochim. Biophys. Acta* **1985**, *811*, 265–322.

(15) (a) Delgado, M. C.; Pigg, K. R.; da, S. F.; Gruhn, N. E.; Sakamoto, Y.; Suzuki, T.; Osuna, R. M.; Casado, J.; Hernández, V.; Navarrete, J. T. L.; Martinelli, N. G.; Cornil, J.; Sánchez-Carrera, R. S.; Coropceanu, V.; Brédas, J. L. *J. Am. Chem. Soc.* **2009**, *131*, 1502–1512. (b) Chen, H.; Chao, I. *Chem. Phys. Lett.* **2005**, *401*, 539–545.

(16) Zhu, L.; Coropceanu, V.; Yi, Y.; Chilukuri, B.; Cundari, T. R.; Brédas, J.-L. *J. Phys. Chem. Lett.* **2013**, *4*, 2186−2189.
(17) Kresse, G.; Furthmüller, J. *Comput. Mater. Sci.* **1996**, *6*, 15−50.
(18) Kresse, G.; Furthmüller, J. *Phys. Rev. B* **1996**, *54*, 11169−11186.
(19) Kresse, G.; Joubert, D. *Phys. Rev. B* **1999**, *59*, 1758−1775.
(20) Perdew, J. P.; Burke, K.; Ernzerhof, M. *Phys. Rev. Lett.* **1996**, *77*, 3865−3868.
(21) Monkhorst, H. J.; Pack, J. D. *Phys. Rev. B* **1976**, *13*, 5188−5192.
(22) Frisch, M. J.; et al. *Gaussian 09*, Revision A.1; Gaussian, Inc.: Wallingford, CT, 2009.
(23) Hay, P.; Wadt, W. *J. Chem. Phys.* **1985**, *82*, 270−310.
(24) Barakat, K. A.; Cundari, T. R.; Rabaâ, H.; Omary, M. A. *J. Phys. Chem. B* **2006**, *110*, 14645−14651.
(25) Zhao, Y.; Truhlar, D. *Theor. Chem. Acc.* **2008**, *120*, 215−241.
(26) Pyykkö, P.; Mendizabal, F. *Inorg. Chem.* **1998**, *37*, 3018−3025.
(27) Couty, M.; Hall, M. B. *J. Comput. Chem.* **1996**, *17*, 1359−1370.
(28) (a) Stephens, P. J.; Devlin, F. J.; Chabalowski, C. F.; Frisch, M. J. *J. Phys. Chem.* **1994**, *98*, 11623−11627. (b) Becke, A. D. *Phys. Rev. A* **1988**, *38*, 3098−3100. (c) Lee, C.; Yang, W.; Parr, R. G. *Phys. Rev. B* **1988**, *37*, 785−789.
(29) Møller, C.; Plesset, M. S. *Phys. Rev.* **1934**, *46*, 618−622.
(30) Schuster, R. E.; Scott, J. E.; Casanova, J. *J. Org. Synth.* **1966**, *46*, 75−77.
(31) Usón, R.; Laguna, A. *Organometallic Syntheses*; King, R. B.; Eisch, J. J., Eds.; Elsevier: Amsterdam, 1986; Vol 3, p 322.
(32) Parks, J. E.; Balch, A. L. *J. Organomet. Chem.* **1974**, *71*, 453−463.
(33) *Bruker APEX2*; Bruker AXS Inc.: Madison, WI, 2007.
(34) *Bruker SAINT*; Bruker AXS Inc.: Madison, WI, 2007.
(35) *Bruker SADABS*; Bruker AXS Inc.: Madison, WI, 2007.
(36) Sheldrick, G. M. *SHELXTL*, v. 2008/3; Bruker Analytical X-ray: Madison, WI, 2008.